Phys. Biol. 18, 046005 (2021), https://doi.org/10.1088/1478-3975/abfa69

A three-dimensional vertex model for *Drosophila* salivary gland invagination

Clinton H. Durney[1]* and James J. Feng[1,2]†

[1]Department of Mathematics, University of British Columbia, Vancouver, Canada
[2]Department of Chemical and Biomedical Engineering, University of British Columbia, Vancouver, Canada

(March 26, 2021)

Abstract

During epithelial morphogenesis, force generation at the cellular level not only causes cell deformation, but may also produce coordinated cell movement and rearrangement on the tissue level. In this paper, we use a novel three-dimensional vertex model to explore the roles of cellular forces during the formation of the salivary gland in the *Drosophila* embryo. Representing the placode as an epithelial sheet of initially columnar cells, we focus on the spatial and temporal patterning of contractile forces due to three actomyosin pools: the apicomedial actomyosin in the pit of the placode, junctional actomyosin arcs outside the pit, and a supracellular actomyosin cable along the circumference of the placode. In an *in silico* "wild type" model, these pools are activated at different times according to experimental data. To identify the role of each myosin pool, we have also simulated various *in silico* "mutants" in which only one or two of the myosin pools are activated. We find that the apicomedial myosin initiates a small dimple in the pit, but this is not essential for the overall invagination of the placode. The myosin arcs are the main driver of invagination and are responsible for the internalization of the apical surface. The circumferential actomyosin cable acts to constrict the opening of the developing tube, and is responsible for forming a properly shaped lumen. Cell intercalation tends to facilitate the invagination, but the geometric constraints of our model only allow a small number of intercalations, and their effect is minor. The placode invagination predicted by the model is in general agreement with experimental observations. It confirms some features of the current "belt-and-braces" model for the process, and provides new insights on the separate roles of the various myosin pools and their spatio-temporal coordination.

Keywords: mechanobiology, salivary gland, cellular intercalation, apical constriction, morphogenesis, tubulogenesis, organogenesis

1 Introduction

Drosophila salivary gland (SG) formation has become a model system for understanding tubulogenesis during embryonic development. In this process, the epithelium invaginates into a protrusion that extends from the plane of the epithelium to form a tube. Each of the two salivary glands, symmetrically located on either side of the ventral midline, forms from a predefined tissue of around 100 cells known as the placode [1–3]. The placodes reside on the anterior domain of the ventral side of the embryo. The formation of the

---

*Current address: John Innes Centre, Norwich Research Park, Norwich, United Kingdom

†Corresponding author. E-mail: james.feng@ubc.ca

tube from a flat epithelial sheet starts at the end of Stage 10 of embryo development and takes about 4 to 5 hours. The process consists of an early stage of placode invagination and tube budding (Stages 11–12) and a later stage of tube elongation (Stages 13–14) [4–7]. The current study focuses on the former. For an elastic finite-element model that investigates the latter, we refer the reader to [8].

During placode invagination, most of the driving forces recognized so far act in the apical plane, yet the gland forms out of the plane. With no cell division or apoptosis, the invagination is realized through cell shape changes and coordinated cellular rearrangements. Recent experiments have uncovered several cellular processes that underlie the observed cell shape changes and rearrangments: a network of apicomedial actomyosin causing apical constriction, increased junctional actomyosin forming contractile arcs and causing cellular intercalation, and a supracellular actomyosin cable surrounding the placode [1–3, 9].

Apical constriction initiates the invagination on a small group of cells in the dorsal-posterior corner of the placode that form the "pit". On the apical surface of these cells, apicomedial myosin forms a web-like structure and pulls on the spot junctions of the cell cortex to constrict the apical cell area [10–12]. During apical constriction, the cell nuclei move basally while the basal domain expands, converting the pit cells from a columnar shape to a wedge shape. The actomyosin complexes are initially pulsatile and anti-correlated with apical cell area [9]. This process helps ensure the proper tissue geometry [3]. However, it has been argued that apical constriction alone is neither necessary nor sufficient for invagination [3, 13]. Apical constriction has been implicated in tissue bending in a variety of developmental scenarios [11, 14–17], a connection that is further supported by biophysical simulations [18–20].

Junctional myosin arises among the placode cells outside the pit. It typically exhibits *planar cell polarity*, being predominantly enriched on tangential or azimuthal cell edges, as opposed to radial edges pointing toward the pit. Thus, it effects anisotropic contraction of the circumferential cell edges [1, 2]. The junctional myosin contributes to SG invagination in at least two ways [2]. First, it aggregates into azimuthally oriented circular arcs that are roughly centered at the pit. Multiple arcs appear that more or less traverse the entire placode, exerting contraction in the azimuthal direction and driving the cells toward the pit. Second, it drives a process of neighbor exchange known as intercalation or T1 transition [21–23]. During this topological change, a cell edge contracts into a four-way vertex and then extends in the orthogonal direction. The net effect within the salivary gland placode is convergence in the azimuthal direction and extension in the radial direction. Occasionally, the contraction of several contiguous cellular edges results in the formation of a rosette [2].

The third and final actor is a supracellular actomyosin cable that surrounds the placode and applies a centripetal force on the cells inside [1, 3, 9]. It forms from linking several previously disconnected actomyosin structures, including the pre-existing actin cables that defined the parasegmental boundaries prior to placode specification, an actin cable running along the ventral midline between the two placodes, and a new actomyosin structure that runs along the dorsal side of the placode. Thus, a continuous belt emerges along the circumference of the placode at the end of Stage 11 and early Stage 12 [1]. Much like the purse-string concept in *Drosophila* dorsal closure [24, 25], the actomyosin cable exerts increasing tension as invagination progresses, pushing the cells toward the pit to feed the growing tube [9].

How do the various myosin pools act in distinct regions of the placode to effect SG invagination? The leading hypothesis is the "belt-and-braces" (BAB) model in which apical constriction at the pit creates braces and the supracellular actin cable serves as a belt that mechanically buckles the tissue [9]. Later work by Sanchez-Corrales *et al.* [2] has added a new factor to the original BAB model: the role of junctional myosin in circumferential constriction, especially via intercalation. This enhanced BAB model provides a useful conceptual framework for placode invagination.

On the above basis, we wish to develop a biophysical model to quantify the roles of the key factors that have been identified during SG invagination: the apicomedial myosin, the circumferentially oriented myosin arcs, cell intercalation and the supracellular actomyosin belt along the periphery of the placode. In this paper, we present a novel three-dimensional (3D) vertex model that captures the apical, basal and lateral

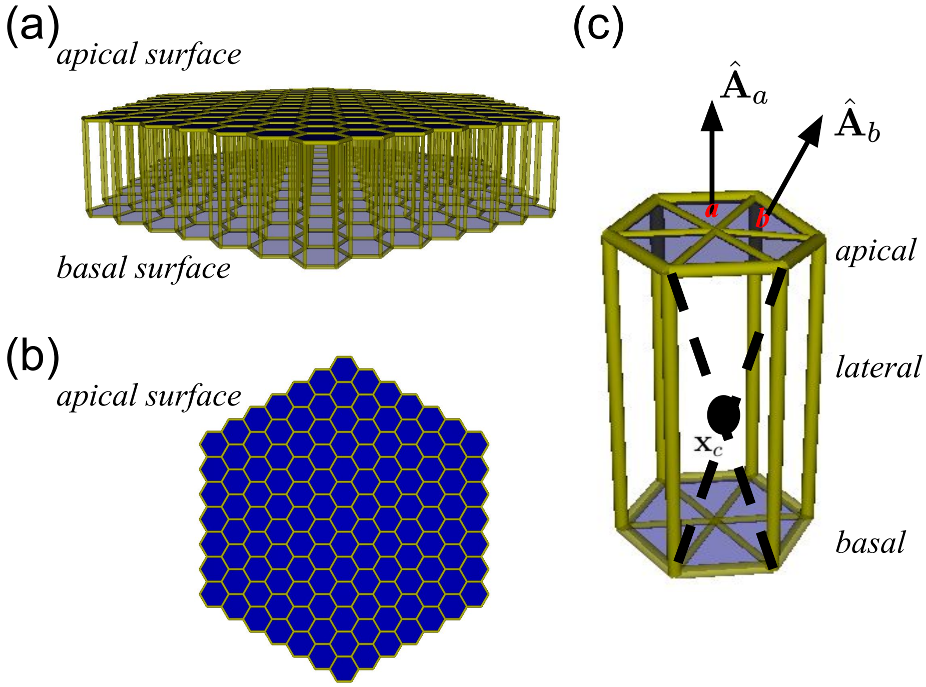

(a)

Figure 1: The 3D vertex model for the salivary gland placode. (a) Side and (b) top views of the placode made up of 127 hexagonal cells. (c) A single cell within the placode consists of 7 apical nodes and 7 basal nodes that are connected by 6 lateral edges. On the apical and basal surfaces, a pressure force acts on each triangular element along its normal vector, and a bending force resists misalignment between the unit normal vectors $\hat{\mathbf{A}}_a$ and $\hat{\mathbf{A}}_b$ of each pair of adjacent triangles a and b. On the lateral faces, we introduce a triangulation by using the centroid $\mathbf{x}_c$ and apply pressure forces on each triangle.

dynamics of cells that constitute the placode. It amounts to an extension and refinement of the BAB model in explicitly accounting for how each pool of myosin affects the shape and depth of invagination.

2 Model Formulation

We represent the salivary gland placode by a 3D vertex model of 127 hexagonal cells (Fig. 1a). The placode itself has an initially hexagonal configuration (Fig. 1b). The apical surface of an individual cell has six peripheral nodes and one central node (Fig. 1c). The peripheral nodes are connected by elastic edges representing the cellular actin cortex, and are connected to the central node by "spokes" that can be taken loosely to represent medial F-actin. The basal topology is a mirror image of the apical surface with the same network connectivity and elastic properties as the apical surface. Corresponding apical and basal nodes are connected with passively elastic lateral edges. Apical and basal edges and spokes are 3.4 μm long in the initial undeformed state [1, 3], and the lateral height is 13.6 μm [2]. Because of the columnar shape of the cells, a fully 3D representation is essential for capturing the invagination of the placode, whose thickness exceeds the diameter of the pit. In addition, relative displacement between the apical and basal surfaces is also a salient feature during invagination [2], including wedging, tilting and potentially interleaving of the cells. Our model builds on prior 3D vertex models [26–30], and can be seen as combining the features of 3D apical vertex models [31, 32] and lateral vertex models [18–20].

Continuum-based mechanical models have been popular in studying other invagination processes such as *Drosophila* mesoderm invagination [33–35] and sea urchin primary invagination [36]. We have chosen a vertex-based representation for the convenience of spatially segregating the various myosin pools, as explained in the next subsection. Another advantage is that the explicit representation of cell edges and cell surfaces will allow relatively straightforward incorporation of biochemical signaling as a future extension to the model. Integrating biochemistry with mechanics has been demonstrated in recent 2D vertex models [23, 37].

2.1 Concentric patterning of forces

As a geometric simplification, we place the pit at the center of the model placode (Fig. 2), instead of in the dorsal-posterior corner as observed *in vivo*. This decision is based on preliminary explorations using an eccentric-pit setup, which are reported in the online Supplemental Information (SI), Sec. S1, with Movies S1–S3. These results suggest that successful invagination in the eccentric setup requires the inclusion of two mechanisms. The first is adhesion between the placode and the surrounding tissue, which should be asymmetrically distributed in space so as to keep the pit from being pulled away from the nearside edge of the placode. At present, modeling the adhesion surrounding the placode is hampered by a scarcity of data on such adhesion forces. The second is a viscous or viscoelastic response in the tissue, due possibly to cortical remodeling [38]. This would afford sufficient fluidity to the tissue so that myosin contraction can drive the large area of placode into the pit in the corner, through frequent intercalations as well as cell deformation [2]. Our current vertex-based representation of the placode is essentially elastic and cannot accommodate such fluidity. The concentric setup is a compromise that alleviates the effects of those two factors, and allows us to use the current model to explore the role of the different myosin pools depicted in Fig. 2.

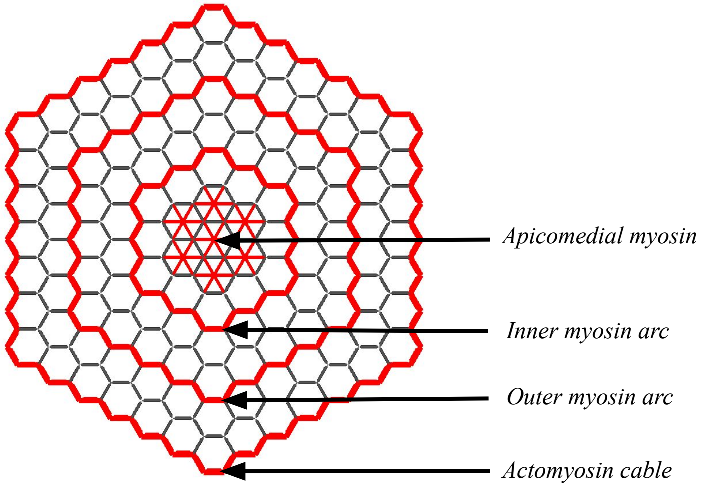

Figure 2: Schematic for the patterning of the active myosin contraction in the concentric *in silico* model of the placode. Apicomedial myosin contracts the apical spokes of the 7 central cells of the pit (colored red), junctional myosin forms 2 actomyosin arcs (red concentric rings) outside the pit, and lastly a supracellular actomyosin cable surrounds the placode (outermost red ring). A cell edge or spoke that is colored red indicates that myosin accumulates on it.

As noted in the Introduction, three active contraction mechanisms have been implicated in salivary gland formation: apicomedial contraction in the pit, junctional myosin contraction outside the pit, leading to actomyosin arcs and intercalation, and contraction of a supracellular actin cable that surrounds the placode.

Each occurs in a distinct region of the placode, in the pit, the bulk, or the periphery of the placode. These are represented accordingly in our model (Fig. 2). Note that the junctional myosin appears to form multiple disconnected myosin arcs *in vivo* [2], and we have represented them by 2 complete rings. The implications of this simplification will be explored further in Subsection 3.2.1. The role of junctional myosin in causing intercalation will be explored separately in Subsection 3.2.2.

Experiments also show that the different pools of myosin onset at 3 different times during Stage 11 of *Drosophila* development [1–3]. The "cells near to the pit", extending roughly 4 cell diameters from the center of the pit, start to contract first, some time before observable invagination [2]. In our model representation, this group includes the pit and the inner myosin arc, and we set their myosin onset at $t = 0$. Then "cells far from the pit", including all other cells in the placode except the periphery, start to experience myosin contraction over 6 minutes later [2]. In our model, we identify these cells with the outer myosin arc, and set its onset at $t = 375$ s. Finally, we have the actomyosin contraction of the peripheral cable starting at $t = 3500$ s. This timing is based on experimental evidence that the peripheral cable becomes complete toward the end of Stage 11, nearly 60 minutes after the onset of the first myosin pool [1, 2, 39]. Note that we view the inner and outer myosin arcs as a single "junctional myosin pool", but have assigned two different onset times to them, the former being synchronized with the pit cells according to experimental evidence [2]. At the onset, a cell edge or spoke is suddenly assigned a certain number of myosin motors, represented in the model by a contractile force on the edge or spoke. The magnitude of this force stays constant on the edge throughout, unless the edge undergoes T1 transition (more details in Sec. 3.2.2). The force on the spokes is somewhat lower than that on the cell edges, according to estimations of cortical and medial myosin motors. Such estimations, along with the evaluation of other model parameters, are detailed in the online SI, with all the model parameters tabulated in Table S1.

In the above, we have specified the spatiotemporal patterning of the myosin contraction in the placode directly. Thus, we have sidestepped the interesting questions of how the patterning emerges under the influence of biochemical signaling pathways, and the kinetics of myosin accumulation and detachment on actin filaments. Biologists have recently started to gather certain insights about the signaling proteins [7, 40]. For example, Fog has been suggested to coordinate apical constriction [3, 7]. In the bulk of the placode, Bazooka accumulates on radially oriented edges, in a complementary pattern to the myosin enrichment on azimuthal edges in planar cell polarity [2]. On the placode boundary, the supracellular actin cable is directed by the myosin activator Rok, which is down-regulated in turn by the apical polarity protein Crumbs [1, 3, 40]. But we are currently far from having enough data for quantitatively modeling the signaling network. Ideally, a mathematical model should integrate the biochemistry upstream and the mechanics downstream for a complete picture of a certain morphogenetic process [23, 37, 41]. Given the dearth of quantitative data of the former, we have decided to focus only on the latter in this study, which to our knowledge will be the first quantitative modeling of SG invagination.

2.2 Governing equations

As is common in vertex models [42–44], we define an energy functional of the tissue for the conservative forces of the system from the position and connectivity of the constituent nodes,

$$E = \sum_{n} \frac{\alpha}{2}(V_n - V_0)^2 + \sum_{i,j} \frac{\mu}{2}(l_{ij} - l_0)^2 + \sum_{a,b} \rho(1 - \hat{\mathbf{A}}_a \cdot \hat{\mathbf{A}}_b) \tag{1}$$

where the index of summation n runs over all cells, (i, j) is over adjacent nodes i and j, and (a, b) is over adjacent areal elements a and b on the apical and basal surfaces (Fig. 1c). The first term represents volume conservation of the cell with pressure coefficient α, with V_n and V_0 being the volume of the n^{th} cell and its rest volume, respectively. The second summation represents the linear elasticity of the edges and spokes with elastic constant μ, l_{ij} and l_0 being the length of the edge or spoke and its rest length. The final summation represents the bending energy of adjacent triangular areal elements a and b on the apical and basal surface, with bending coefficient ρ and unit normal vectors $\hat{\mathbf{A}}_a$ and $\hat{\mathbf{A}}_b$, respectively. The inclusion of the bending energy is common in apical vertex models [31, 32, 45] but not in 3D vertex models [26, 29, 30]. In our model, bending elasticity serves to inhibit short-wave buckling of the apical sheet, as illustrated in Sec. S4 of the online SI.

The conservative forces on node i can be computed from the energy as

$$\mathbf{F}_i^{\text{con}} = -\nabla_i E, \tag{2}$$

where ∇_i is the gradient operator with respect to the nodal position $\mathbf{x}_i$. The three terms of E thus yield, respectively, a pressure force, a passive elastic force and a bending force. Detailed expressions can be found in the online SI.

Of course, the interesting dynamics of the placode is driven not by the *passive* elastic relaxation dictated by E, but by *active* contractile forces due to myosin. The junctional myosin force will be posed on cell edges, while the apicomedial myosin prevails on the spokes of the inner cells making up the pit. The supracellular cable exerts contraction on the edges along the placode's circumference. Assuming overdamped dynamics [37, 46], we write the equation of motion of node i as

$$\eta \frac{d\mathbf{x}_i}{dt} = \mathbf{F}_i^{\text{con}} + \mathbf{F}_{ij}^{\text{myo}}, \tag{3}$$

where η is the friction coefficient, and $\mathbf{F}_{ij}^{\text{myo}}$ represents the active force due to myosin on the edge between nodes i and j. Inside the cellular micro-environment, there are multiple mechanisms for dampening nodal motion, including viscous friction, cell-cell adhesion and, in the later stage of invagination, cell-ECM adhesions. For simplicity, these effects are combined into a single "viscosity" parameter η. The myosin force is nonzero only if node i belongs to one of the myosin pools of Fig. 2 (more details in SI). Initially, the placode is tension-free with all edges and spokes at their resting length. With the onset of myosin forces, the vertices move according to Eq. (3), causing the edges to contract, move or reorient. Note that the placode is subject to no external forces along its edges. Thus, as the placode invaginates, its center of mass stays fixed in space.

In our numerical simulation, Eq. (3) is advanced in time using the forward Euler scheme with a sufficiently fine time step Δt. Details of the numerical implementation are described in Sec. S5 of the online SI.

3 Results

Using the concentric placode geometry, our model is able to demonstrate the main features of salivary gland invagination. First, we consider a placode with all pools of myosin shown in Fig. 2 activated at their respective time of onset. We consider this an "*in silico* wild type" (WT) placode. We then compare this baseline scenario against "*in silico* mutants" in which we isolate each of the pools of myosin. For example, we can retain only one myosin pool while deactivating the other two pools, or deactivating that pool while retaining the other two. By comparing such mutants with the WT, the role of each pool can be clearly delineated. We will present and analyze the model predictions according to the following scheme: (a) Qualitative description of the *in silico* WT placode; (b) Quantification of the contribution of various myosin pools through *in silico* mutants; (c) Comparison with *in vivo* experiments. In quantifying the model predictions and comparing with experimental data, we will use the width and depth of the invagination as well as the width of the pit. These geometric measures are defined in Sec. S6 of the SI.

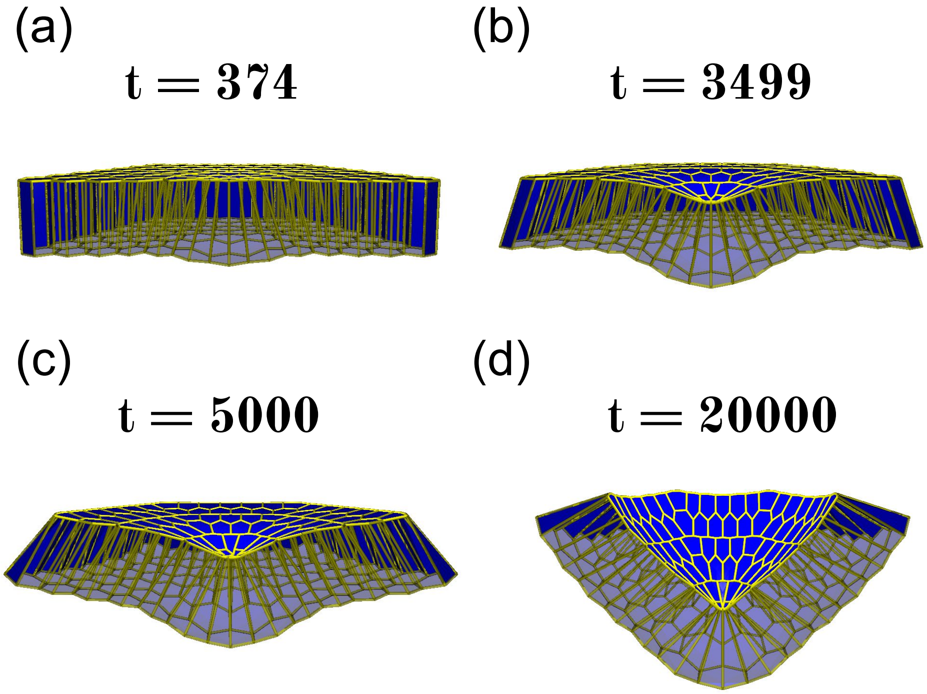

Figure 3: Snapshots of the *in silico* WT placode during invagination, showing the mid-plane crosssection as well as half of the tissue behind the cross section. (a) The apicomedial myosin and the inner myosin arc activate at $t = 0$ s and are the only active forces deforming the tissue until $t = 375$ s. The pit begins to bulge out at the center of the placode, and the surrounding cells start to tilt. (b) The outer myosin arc activates at $t = 375$ s and drives the pit further into the embryo. (c) An intermediate shape at $t = 5000$ s. After the peripheral belt activates at $t = 3500$ s, all three myosin pools are actively contracting. (d) An equilibrium state is achieved around $t = 20000$ s, with the placode invaginated into a dome-like shape.

3.1 Qualitative description of the *in silico* wild-type concentric placode

Figure 3 shows four snapshots of the *in silico* WT placode as it invaginates into a conical shape. The sequence of cell shape changes include the establishment of a pit and initial tissue bending (Fig. 3a,b), further deepening of the pit (Fig. 3c), and formation of a lumen and invagination into the final shape (Fig. 3d). The dynamic process can be viewed in Movie S4 of the online SI.

The initiation of invagination is due to the onset of myosin on the apicomedial domain of the cells in the pit and on the inner myosin arc. In the pit, we see a constriction of the apical cell surface and a bulging of the basal domain (Fig. 3a). Because the contraction is spatially localized to the pit and the inner arc, the amount of deformation remains small before the onset of the outer myosin arc at $t = 375$ s. The volume conservation term of Eq. (1) induces an internal pressure within the cells that expands their basal portion, causing the cells to become wedge-like. The transition from initially columnar cells into wedge-shaped cells is a known precursor to tissue bending in a variety of epithelial and developmental contexts [11, 14–17].

The onset of the outer myosin arc produces a tissue-scale compressive force on the interior portion of the placode that pushes the apical nodes inward and further establishes the pit at the geometric center (Fig. 3b). As the active forces are only on the apical surface, the centripetal movement of the apical nodes precedes that of the basal nodes, as the latter are only driven by forces transmitted through the lateral elastic edges. This results in cell tilting, which is more pronounced than at the earlier snapshot. Another effect of

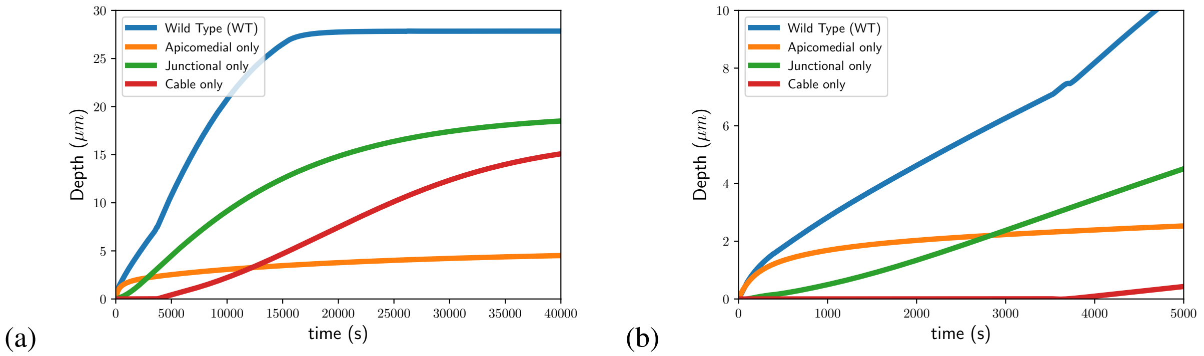

Figure 4: Comparison between the *in silico* WT placode and the three *in silico* mutants. (a) Temporal evolution of the depth of invagination. The depth is measured from the basal cell face of the central cell to the lip of the tube (details in online SI, Sec. S6). For the mutants, the final shape takes longer to reach than the time period plotted. (b) A magnified view of the early phase of invagination. The kink in the WT curve is a response of the placode to the onset of the peripheral cable, occurring shortly after the cable's onset at $t = 3500$ s. It can be seen more clearly in the online Movie S4.

the junctional myosin is that it tends to align the cell edges on which it resides. Such straight boundaries are visible in Fig. 3(b–d). Similar aligned boundaries have been reported *in vivo*, for example in Fig. 7 of Sanchez-Corrales *et al.* [2].

The activation of the peripheral actomyosin belt provides immediate help to the ongoing invagination. The first noticeable effect of the peripheral cable is to round the corners of the placode, rendering its border smoother and increasing its circularity. This effect has been observed *in vivo* [1, 3], and resembles that of another supracelluar cable during *Drosophila* dorsal closure [37, 47]. Afterwards, the belt exerts a radial constriction that is similar to that of the two interior myosin arcs: furthering inward movement of the apical nodes, driving the pit downwards, and augmenting cell tilting (Fig. 3c). At this stage, the wedging and tilting of the cells, mediated by edge elasticity and cytoplasmic pressure, naturally require the outer edge of the basal surface to move upward. Eventually, the basal surface curls up to form the outer surface of the tube while its edge forms the lip of the tube (Fig. 3d). As the pit is further driven into the embryo, the circumferential belt constricts the opening of the tube and facilitates the transition to the final dome-like morphology.

3.2 Quantification of the roles of the different myosin pools

The SG invagination described in the above involves the contractile action of three myosin pools. To quantify their individual roles, we compare the *in silico* WT model with three *in silico* "mutants". In each mutant, we activate one of the pools of actomyosin with the others turned off. The first mutant has only apicomedial actomyosin, the second only junctional actomyosin in the form of two myosin arcs, and the third only the peripheral actomyosin cable. We refer the reader to Fig. 2 for the positioning of the various myosin pools. In all scenarios, we allow the simulations to run until the placode has reached a steady-state shape. The mutants require a longer simulation time than the WT as the reduction in active forces slows down nodal dynamics. This is consistent with the *in vivo* observation that blocking apical constriction in a mutant resulted in a delayed invagination process [3]. In addition, we have also tested mutants with two of the three pools of myosin intact and the third inactivated. The results, reported in the SI, Sec. S7, are consistent with the results presented below.

The temporal dynamics of the invaginated depth are reported in Fig. 4. The WT invaginates the deepest.

The mutant with just the junctional actomyosin arcs invaginates to about 2/3 of the WT depth. The mutant with only the peripheral actomyosin cable invaginates roughly half of the WT, and that with only the apicomedial actomyosin invaginates the shallowest. Next we analyze the roles of different myosin pools by exploiting their staggered timing of activation.

In the WT placode, the initial stage of invagination is driven by the apicomedial contraction in the pit and the two junctional myosin arcs, the inner arc starting to contract at $t = 0$ with the apicomedial myosin in the pit and the outer arc being activated at $t = 375$ s. Prior to $t = 375$ s, the apicomedial-only mutant lacks the inner myosin arc in comparison with the WT. But this turns out to be a minor handicap as the apicomedial contraction in the pit alone produces most of the WT depth before the onset of the second myosin arc (Fig. 4b). In contrast, the junctional-only mutant, with only the inner myosin arc active before $t = 375$ s, attains only about 10% of the WT depth at $t = 375$ s. Thus, the inner myosin arc is not nearly as effective as the apicomedial contraction in the pit. The trend is reversed after the outer myosin arc starts contraction at $t = 375$ s. The junctional-only mutant catches up with the apicomedial-only mutant around $t = 2800$ s, and proceeds to invaginate to a final depth that is 2/3 of that of the WT. The apicomedial-only mutant, on the other hand, settles into a very slow and mild contraction, achieving only about 16% of the WT depth in the end.

The relative weakness of the apicomedial myosin in driving invagination reflects the limited spatial dimension of the pit. The apicomedial contraction atop each pit cell is powerful as it occurs on 6 spokes per cell. But the 7 pit cells have to pull the entire expanse of the placode inward. In comparison, the myosin arcs are more effective as they constrict a wider portion of the placode, even though the contractile force acts only on a single edge of any cell next to the arcs. Interestingly, the two pools of myosin appear to exhibit “synergy”. Working together in the WT, they produce an invagination depth greater than the sum of those due to each alone. This is true even before the peripheral actomyosin cable onsets at $t = 3500$ s. Although the apicomedial myosin does not contribute much to the overall depth, it creates the initial tissue bending at the pit that allows the myosin arcs to drive the nadir down more rapidly and effectively. Such collaboration between the myosin pools is consistent with the essence of the belt-and-braces model [2, 9]. It is manifested even more clearly by a new mutant that lacks the apicomedial myosin but retains the other two myosin pools. See Sec. S7 in the SI for details.

Upon its onset at $t = 3500$ s, the peripheral actin cable provides an immediate boost to the rate of invagination of the WT placode, bending the curve upward in Fig. 4. The cable-only mutant only starts to invaginate after $t = 3500$ s, and at a rate much lower than the WT at the same time. This is because it lacks the apicomedial and junctional myosin that would have generated an initial invagination in the center to facilitate further constriction by the peripheral cable. In fact, the cable-only mutant invaginates at a slower initial rate than the junctional-only mutant, probably because its constriction has to contend with the elastic and viscous resistance of the entire placode. In the end, the cable-only mutant invaginates to about half of the WT depth.

To further examine the role of the peripheral cable, we have also tested a new *in silico* mutant by turning off the peripheral cable while retaining the other two pools of myosin (see Sec. S7 in the SI for details). Such a mutant achieves about 78% of the WT depth (Fig. S7a), and thus the cable does contribute substantially to deepening the invagination in the WT. In addition, the cable has another benefit in shrinking the opening of the invagination and increasing its depth-to-width aspect ratio (Fig. S7b). In comparison with the mutant lacking the peripheral cable, the WT produces an opening that is 7% narrower, and an aspect ratio 38% greater. This underscores the vital role that the peripheral belt plays in constricting the opening of the invagination and shaping its final geometry, a role noted in association with Fig. 3(d) already.

By comparing the final morphology of the placode among the WT and the mutants in Fig. 5, we can distinguish the roles of the various myosin pools. The apicomedial actomyosin only creates a small dimple at the center, and the placode fails to invaginate further (Fig. 5b). The mutant with only the two myosin arcs is able to fully internalize, but fails to form a proper lumen (Fig. 5c). The base of the invagination opens

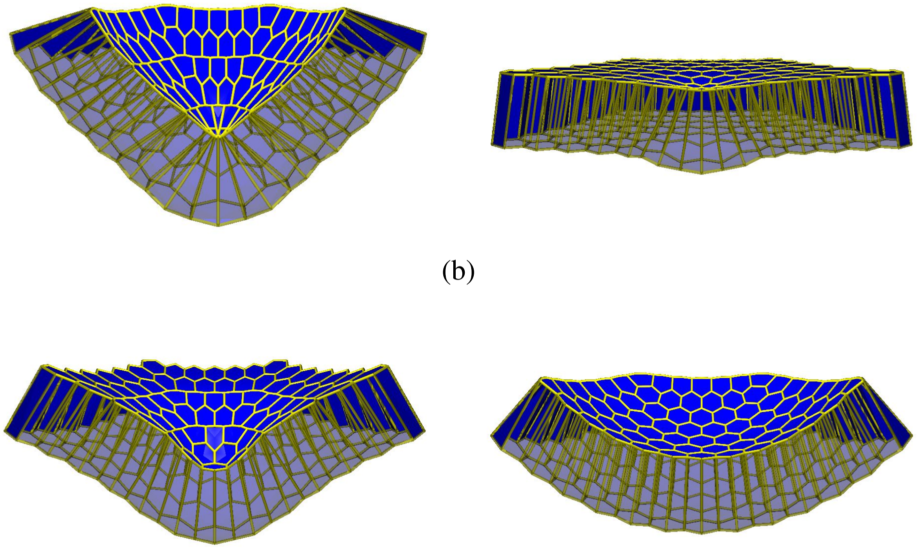

(a) (b)

(c) (d)

Figure 5: Cross-sectional views of the morphology at $t = 40000$ s of the placode for (a) the WT, (b) the apicomedial-only mutant, (c) the junctional-only mutant and (d) the peripheral cable-only mutant.

widely. The mutant with only the peripheral actomyosin cable attains a much shallower invagination and is much wider than the WT placode (Fig. 5d). To sum up the WT invagination process, the apicomedial myosin forms a small dimple at the start, but its effect is soon overshadowed by the junctional myosin arcs. The myosin arcs are the main driver of invagination and are responsible for the internalization of the apical surface. The peripheral actomyosin cable is responsible for forming a properly shaped lumen and constricting the opening on the apical surface. This picture shares some commonalities with the BAB model, and also has its own distinctive features. We will return to this point in Sec. 4, Discussion.

So far, we have modeled the junctional myosin as two concentric myosin rings. Two *in vivo* features have been neglected: that the junction myosin form disjointed partial arcs instead of complete rings, and that they also induce intercalation. The latter, in particular, plays a role in SG invagination that has been documented experimentally [2]. The following two subsections will examine these two factors in turn.

3.2.1 Discontinuous myosin arcs

The myosin arcs are discontinuous *in vivo* (see Fig. 7 in [2]). To test the effect that this may have on the invagination dynamics, we have designed three patterns of discontinuous actomyosin arcs in Fig. 6(a). The inner myosin ring stays continuous, and the outer ring is replaced by disjointed segments that are offset radially in different ways. The other two pools of myosin, the apicomedial in the pit and the cable along the periphery, are kept as in the *in silico* WT.

There is very little difference among the four scenarios in the invaginated depth of the placode; all 3 discontinuous cases fall within 1 % of the wild type placode (Fig. 6b). Arc 3 has slightly deeper invagination during much of the process, but the difference diminishes in time in the final phase of invagination. In the end, Arc 3 produces a slightly deeper (by 0.18 μm) invagination than the wild type. The advantage of Arc 3 over the other discontinuous arcs may be because it has continuous segments around all of the six corners of the hexagonal placode, and are thus better able to constrict the placode. In comparison to the continuous

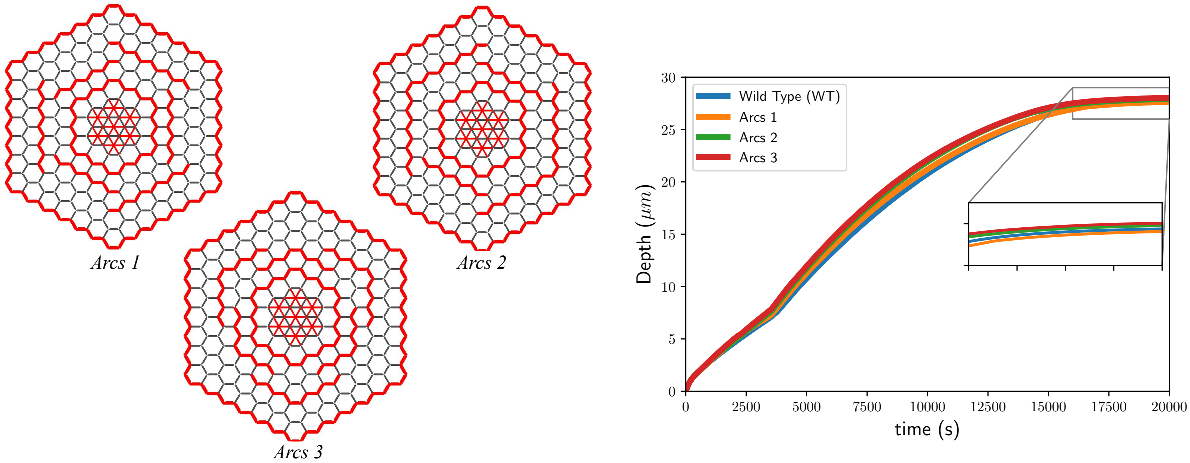

(a)

(b)

Figure 6: (a) Patterning of the three discontinuous myosin arcs. (b) Comparison of the depth of invagination between the discontinuous myosin arcs and the continuous myosin arcs in WT.

outer arc of the wild type, the inward shift of some of the disjointed segments may have been more apt at providing a pushing force downwards due to their proximity to the pit. Given the insignificance of the myosin arc configuration, we will continue to use the simple continuous myosin rings in the WT.

3.2.2 Quantifying the role of intercalation

Cellular intercalation in the placode consists mainly in junctional shortening in the circumferential direction followed by junctional elongation in the perpendicular radial direction [2]. This is schematically illustrated in Fig. S8 of the online SI. Conceivably, therefore, intercalation can promote cell movement from the periphery toward the pit and facilitate the invagination. As is well known in germband extension, cell intercalation is preceded by planar cell polarity governed by anisotropic enrichment of various proteins (e.g. Rho-kinase, Bazooka and E-Cadherin) among edges in different orientations [22, 23]. In keeping with the treatment of the other myosin pools, we will omit the biochemical signaling and pose the anisotropic myosin contraction forces directly as follows.

We prescribe a number of circumferential edges in the belt of cells between the two myosin arcs for intercalation (Fig. 7). We have tested 4, 6, 8 and 12 intercalations and they are more or less uniformly distributed along the same circumferential ring. The myosin onsets on these edges at the same time as on the outer myosin arc ($t = 375$ s), but with a contractile force that is 33% larger to ensure that the edge shrinks quickly to a threshold length at which we realize the T1 transition by reorienting the short edge into the radial direction and reconnecting its ends to the surrounding nodes. More details about the implementation of cell intercalation are given in the SI, Sec. S8. Afterwards, the new radial edge will carry no myosin for the remainder of the simulation to comply with the planar cell polarity of the tissue [22, 23]. Although all of the intercalating edges start their contraction at the same $t = 375$ s, the intercalation may not occur at exactly the same times given geometric differences and cell-cell neighbor interactions. They typically occur within a narrow time window of 12 s. The online Movie S5 shows the dynamic process of invagination with 4 intercalating edges.

As before, we compare the temporal evolution of the invaginated depth for the various cases (Fig. 8). As the number of intercalations increases from 0 to 4 and then to 6, the depth of invagination increases progressively, albeit by a relatively small amount. This trend is consistent with *in vivo* observations, but the

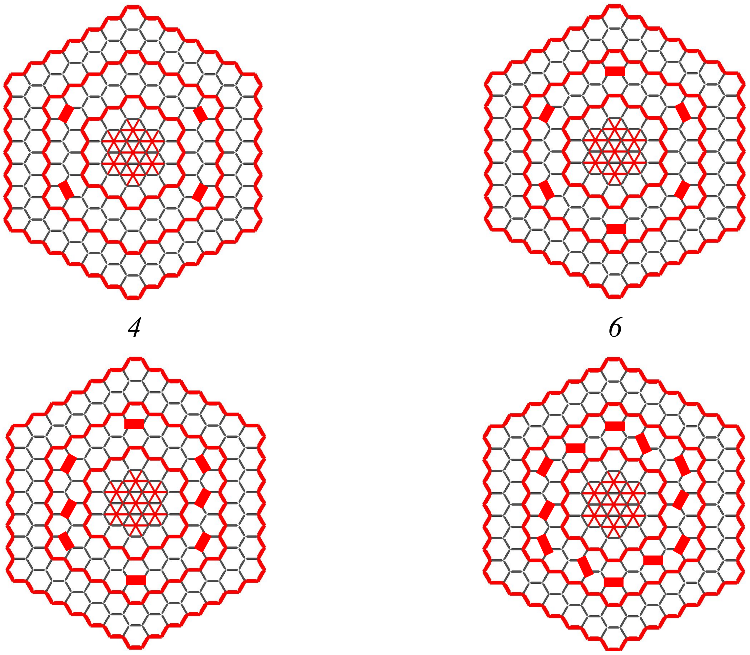
4 *6* *8* *12*

Figure 7: Patterning of junctional myosin on selected edges designated for intercalation, marked by thick red line segments, with 4, 6, 8 and 12 intercalations. Under myosin contraction, these edges will shrink in the circumferential direction to a point and then elongate in the orthogonal direction.

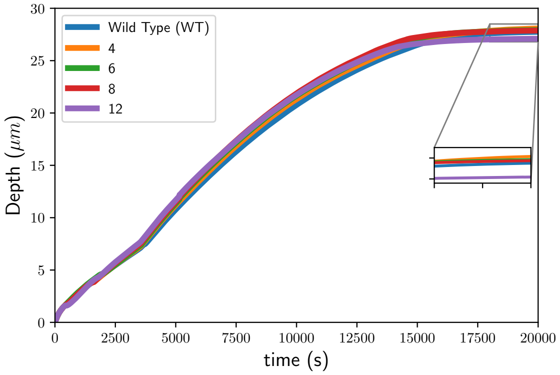

Figure 8: Role of intercalation on the SG invagination depth. In the end, a placode with 6 intercalations invaginates the deepest followed by 4, 8, then the wild type and lastly, the 12 intercalation placode invaginates the shallowest.

benefit is much smaller than reported by Sanchez-Corrales *et al.* [2] (Fig. 2E therein). Surprisingly, for 8 and more intercalations, the effect appears to be reversed and the 12-intercalation case performs slightly worse than the wild type simulation. Analyzing the images, we discover that the larger number of intercalations tend to cause such an intense radial squeeze that some cell edges are liable to rotate in the plane in a kind of local "buckling". Afterwards these edges are no longer oriented towards the pit nor contributing as much to the invagination.

The underprediction of the effect of intercalation, relative to *in vivo* observations [2], is a limitation of our vertex-based model of the placode. The tissue appears to be much more fluid-like *in vivo*, undergoing over 200 neighbor exchanges in favor of radial extension and over 100 reverse ones in favor of circumferential extension [2] (Fig. 5C therein). With cell-cell connection represented by vertices and elastic edges, the placode *in silico* appears much more rigid and less capable of accommodating intercalations. Cell intercalation plays an important role *in vivo* in constricting the tissue circumferentially and extending it radially into the pit [2]. The unrealistically wide lumen observed *in silico*, e.g. in Fig. 3, may be a direct consequence of the model's inability to accommodate sufficient numbers of intercalations. Interestingly, softening the elastic coefficient μ can result in spontaneous intercalations and a narrower lumen (Fig. S5 and Movie S6 in the SI). As an *ad hoc* measure to reduce the elastic resistance *in silico*, this is consistent with the argument for greater tissue fluidity and deformability.

The *in vivo* fluidity may be related to cortical remodeling inside each cell, which occurs on a time scale of minutes [38], much shorter than that of the placode invagination. The cortical turnover thus amounts to a viscous response that allows the cells to adopt new shapes relatively quickly in response to external forcing [48]. Conceivably, a viscoelastic model that accounts for cortical remodeling may reduce the energetic barrier in our purely elastic vertex model and facilitate intercalation [49]. Thus, realistic representation of intercalation is an open question for future vertex-based modeling.

3.3 Comparison with experimental observations

Despite the relative simplicity of our mechanical model, it captures a number of qualitative features observed *in vivo*. For example, the model placode exhibits wedging of cells at the center of invagination (Fig. 3a,b), and tilting of cells further from the invagination pit (Fig. 3c). The model also suggests that cellular intercalation is an active process driven by myosin contraction on the intercalating edge, as opposed to a passive one induced by neighboring cells deforming and moving. These observations are in agreement with *in vivo* observations [2, 3, 5].

For more quantitative comparison, we find a wealth of experimental data on the apical area changes in the placode [2]. Sanchez-Corrales *et al.* [2] divided the placode into five roughly concentric stripes, with "cells near the pit" being Stripe 1 and the peripheral cells being Stripe 5, and reported the areal evolution within each stripe for the first 30 min after contraction starts at the pit. Accordingly, we identify in our model the 19 cells inside the innermost myosin arc (see Fig. 2) with their Stripe 1, our "bulk of the placode", i.e. the next 3 concentric rings of cells, with their Stripes 2–4, and finally our peripheral ring of cells with their Stripe 5. The areal change during the initial stage of invagination are compared in Fig. 9 between the *in silico* WT placode and the *in vivo* placode.

The cells near the pit contract monotonically and relatively rapidly both *in silico* and *in vivo* (Fig. 9a). Our model makes the simplifying assumption of instant myosin onset at $t = 0$, whereas in reality, the myosin builds up gradually in time. This explains the faster initial contraction in the model prediction. But overall the contraction rate is comparable between the two. In the bulk of the placode (Fig. 9b), the model predicts an initial areal increase as the radially inward contraction at the pit enlarges the surrounding cells. Upon the activation of the outer arc at $t = 375$ s, the trend is reversed and the bulk exhibits a gradual decline. The *in vivo* placode shows no such reversal, but only changes in the slope. This is probably because the *in vivo* placode, unlike its *in silico* mimic, does not have an abrupt and simultaneous onset of myosin around a complete myosin arc. Within Stripes 2, 3 and 4 that make up the bulk of the placode, junctional myosin onsets in a more stochastic manner both temporally and spatially, thus yielding a gradual areal shrinkage of the bulk region. The overall contraction rate is again close between the simulation and experiment. Finally, the periphery shows an initial expansion in both cases (Fig. 9c), owing to the inward pulling of the junctional and apicomedial myosin pools. The circumferential actomyosin cable will not become active until $t = 3500$ s. In the model prediction, the onset of the outer arc at $t = 375$ s has a sudden effect in enlarging the peripheral cells. Afterwards, the peripheral cells contract elastically as the tissue adapts to the myosin arc,

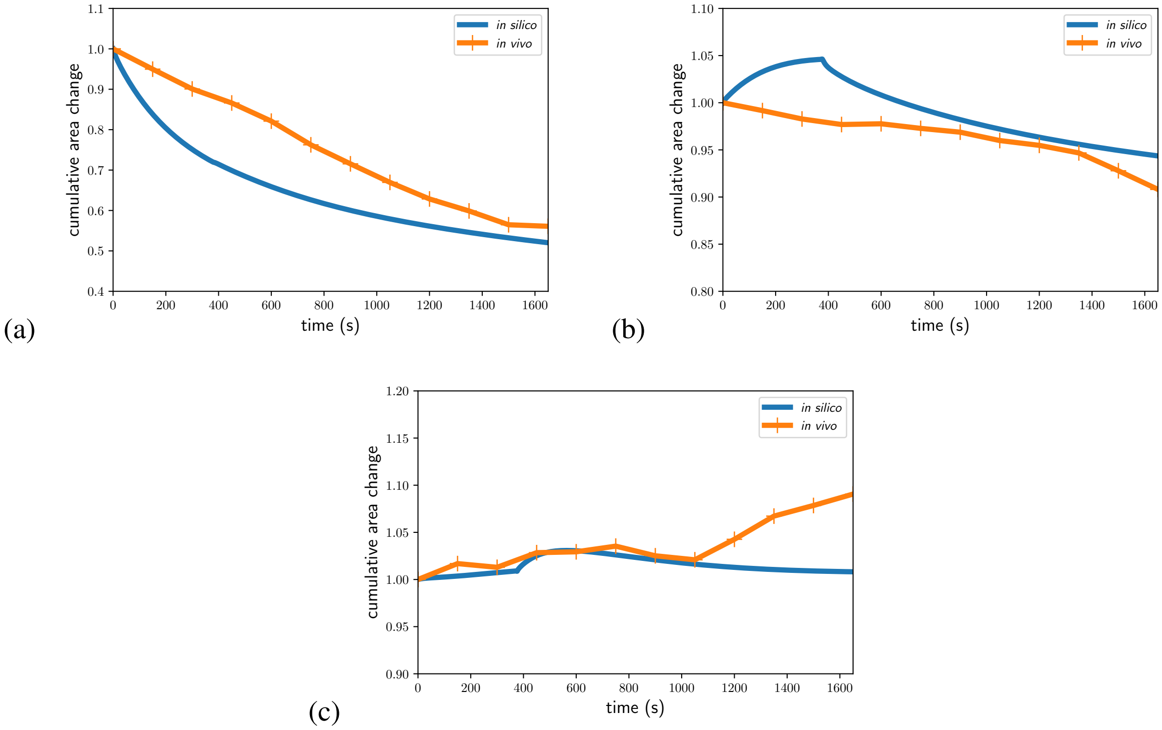

(a) (b) (c)

Figure 9: Comparison of the *in silico* and *in vivo* apical area changes in three regions of the placode. (a) Cells near the pit. (b) Cells that make up the “bulk of the placode”. The *in vivo* data are averaged over Stripes 2–4 of Sanchez-Corrales *et al.* [2]. (c) Peripheral cells. All areas have been normalized against their initial values at the first reported time point.

resulting in a slight decline in cell area over time. For reasons given above, the *in vivo* cells react in a less drastic manner. They lack the sudden expansion seen in the model, but overall the areal expansion is more pronounced *in vivo* than predicted. To sum up the comparison in Fig. 9, the model captures the general trend in cell area variations in different regions of the placode, but with discrepancies in certain fine features. This is attributable to the vertex-based geometry of the model and the simple representation of elastic and viscous resistance to cell deformation.

In addition, we can compare the *in silico* mutants with the *in vivo* mutants (Fig. 10). Chung *et al.* [3] over-expressed a constitutively active form of Diaphanous (Dia-CA) protein to block actomyosin contraction on the apical surface throughout the placode. Under the compressive force of the peripheral cable, invagination still occurred. But the mutant showed a shallower invagination depth, a wider luminal diameter, and an apical surface area distribution biased in favor of larger cells. This can be compared with our *in silico* mutant of Fig. 5(d), where the apicomedial myosin in the pit and the junctional myosin arcs are both suppressed, leaving the peripheral actomyosin cable as the only active contractile element. The result is a shallow and wide invagination. This can also be appreciated from the width of the pit (defined in Sec. S6 of online SI). The cable-only mutant displays a much wider pit than the WT (Fig. 10a), in agreement with the observations of Chung *et al.* [3] (Fig. 6 therein). Moreover, its apical area distribution is shifted significantly toward larger cells relative to the WT (Fig. 10b), in qualitative agreement with *in vivo* data (Fig. 5I of [3]).

Chung *et al.* [3] also studied a *fog* mutant, in which the cells featuring apicomedial constrictions are no longer concentrated at the pit, but are distributed randomly over the whole placode. The apicomedial myosin concentration is also reduced by a factor of 2.5 relative to the WT. The *fog* mutant invaginates and

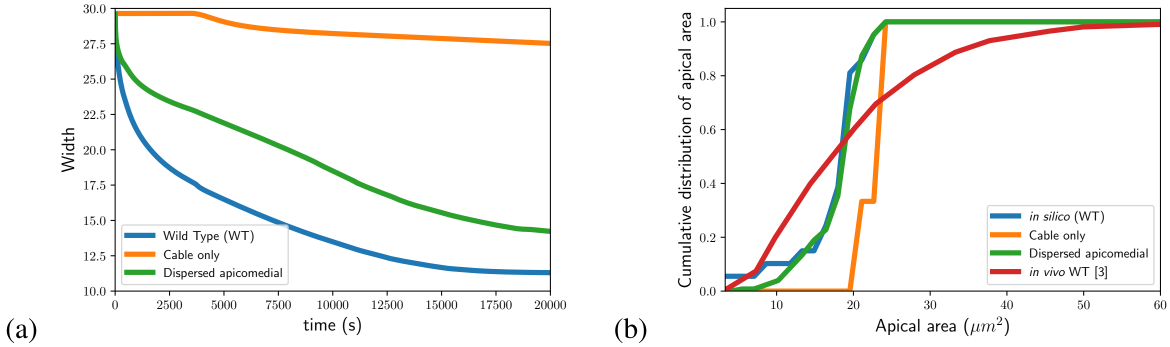

Figure 10: Comparison between *in silico* model predictions for the WT and two mutants. The "cable only" mutant mimics the Dia-CA mutant *in vivo*, and the "dispersed apicomedial" the *fog* mutant *in vivo*. (a) The WT shows a narrower pit than the two mutants. The width of the pit is defined in the online SI, Fig. S6. (b) Cumulative distribution of the apical area. The "cable only" mutant displays a distribution shifted toward larger cells, while the "dispersed apicomedial" mutant has a similar distribution to the WT. Also included is the *in vivo* data from [3] which shows a wider distribution than the model prediction.

achieves roughly the same area distribution as the WT. But the pit is wider. We recreated this mutant by redistributing the seven "pit cells" that experience apicomedial constriction randomly throughout the tissue and decreasing the contractile force on the apical spokes by the factor of 2.5. This *in silico* mutant exhibits a pit width that is wider than the WT but narrower than the cable-only mutant (Fig. 10a). Its distribution of apical areas is essentially identical to that of the WT (Fig. 10b). Both predictions agree with experimental data (Figs. 4CD and 6AB of [3]). Because only the few pit cells are affected in the "dispersed apicomedial" mutant, the small differences are not surprising. But for the mutant, the most constricted cells, say those with an apical area below 10 μm^2, are fewer in Fig. 10(b), as the pit cells now have larger apical areas on account of the reduced apicomedial myosin.

We have also compared the cumulative distributions of apical areas between the *in silico* model and *in vivo* data of Chung *et al.* [3], for WT and the various mutants. In all cases, the model predicts a narrower distribution than the *in vivo* data; Fig. 10(b) shows such a comparison between the *in silico* WT and *in vivo* WT data. This is probably because the vertex model has regular geometry with uniform cell area at the start. It also lacks the cellular remodeling *in vivo* that may introduce greater variations in cell area. The same trend can be seen in comparing the apical areal distributions for *in silico* and *in vivo* mutants (data not shown).

4 Discussion

The objective of this work is to create a quantitative and predictive model of invagination of the *Drosophila* salivary gland placode based on experimental findings of force generation and transmission. To do so, we develop a novel 3D vertex representation of the cellular dynamics of placodal cells, including deformation of the apical, basal and lateral surfaces. According to experimental observations of the patterning of forces, the model includes three pools of actomyosin, the apicomedial in the pit, the junctional outside the pit, and the peripheral along the circumference of the placode. Thus, we are able to test *in silico* "mutants" that mimic *in vivo* mutants, e.g., mutants with only apicomedial myosin in the pit [1, 3], only junctional myosin [2], or only the circumferential actin cable [1, 3, 9]. This allows us to delineate the role played by each myosin pool in driving the morphogenetic movements. Using model parameters estimated from available data in the literature, our model has predicted the following main results:

- The salivary gland invaginates under the orchestrated action of contractile forces due to three pools of myosin.
- Apicomedial actomyosin causes apical constriction and early tissue bending in the pit, but contributes little to the later stages of invagination.
- The junctional myosin arcs outside the pit are the main driver of invagination. They provide most of the radial forces that push the cells inward toward the pit and downward into the budding tube.
- Cell intercalations aid in invagination, but our 3D vertex model can only accommodate a smaller number of them, with a relatively minor effect on invagination.
- The supracellular actin cable surrounding the placode is not necessary for the internalization of placodal cells, but plays a unique role in constricting the opening of the invagination.

These predictions are in general agreement with experimental observations of wild type and mutant fruit flies. For example, the model confirms the observations of Chung *et al.* [3] that the apical constriction in the pit helps define the tip of the tube but is not essential to the success of invagination. It also supports the argument for an active cause for cell intercalation [2]. That is, cells intercalate through local active myosin contraction along the circumferential edges as opposed to passive tissue stretching over a large area of the placode. Our model recapitulates mutant placodes absent apical constriction that form shallow invaginations [3]. It captures the temporal evolution of cell areas in different regions of the placode and cell shape changes near the pit [2], as well as the changes in the cell area distribution in various mutants [3].

Incidentally, the process of dissecting the role of different myosin pools showcases two advantages of the 3D vertex model. First, it is easy to specify and manipulate myosin pools at different spatial locations in the model placode, even on distinct cell edges in the tissue. In comparison with continuum-based modeling, this relates more directly to the real placode *in vivo*. Second, the model can test various *in silico* mutants readily, and this greatly facilitates the identification of roles of different myosin pools. Some such mutants are difficult or impossible to realize *in vivo*, an example being a mutant placode with all myosin pools except the peripheral cable.

Booth *et al.* [9] proposed the belt-and-braces (BAB) model in which the apicomedial myosin and circumferential actin belt coordinate to affect invagination of the placode. This framework was later amplified by Sanchez-Corrales *et al.* [2] with new data showing how junctional myosin contributes to invagination. To reconcile our model with this enhanced BAB model, we first note that our model also predicts a prominent role for the junctional myosin. In fact, it is the main driver for the circumferential constriction of the placode. Second, it confirms the importance of the circumferential actomyosin cable and identifies a special role for it, not so much in driving the in-plane cell motion toward the pit but in improving the tissue geometry. It helps raise the rim of the invagination and narrow its opening. Finally, the *in silico* model indicates a smaller role of the apicomedial contraction in the pit, consistent with findings by Chung *et al.* [3]. Even in the absence of the initial pit depression, tissue buckling and invagination will occur, albeit with a delay, once the junctional myosin starts to constrict in a polarized fashion along azimuthal arcs. Relative to the enhanced BAB model, one can say that our model assigns a smaller role to the apicomedial myosin in the pit and a somewhat different one to the circumferential actin cable that surrounds the placode.

We end by noting the limitations in the current model. As with any modeling of complex biological processes, ours employs a number of simplifications and assumptions. First, the model has completely neglected biochemical signaling that controls and regulates the invagination. For example, the spatial patterning of the myosin pools in the placode appear to be controlled by the transcription factors Hkb and Fkh [7]. In cells far from the pit, circumferential-radial polarization of the placode is controlled by Baz/Par3, which sets the stage for intercalation and the myosin arcs [2]. Additionally, the actomyosin contractions are Rho1 dependent and show pulsatile behavior [1], reminiscent of other morphogenetic processes in *Drosophila* embryos [37, 50]. Recent experiments suggest a role of Crb for modulating Rok on the placode border and controlling the circumferential belt formation [40]. We have neglected all such upstream pathways and postulated myosin accumulation *ad hoc*. In modeling similar processes such as germband extension [22, 23] and dorsal closure [37], linking biochemical signals to mechanical deformation has greatly aided our understanding of the polarization and morphogenesis of tissues. In this sense, we have only focused on the mechanical aspect, and a complete model integrating mechanics with biochemistry remains to be developed for SG tubulogenesis.

Second, we have adopted various geometric simplifications in our 3D vertex model. Foremost among these is the concentric patterning of myosin pools with the pit at the center. In comparison with the eccentric pit, the concentric pit may have amplified, to some degree, the constrictive role of the junctional myosin arcs, and also affected the kinematic and geometric features of the cell movement. Recent work by Sanchez-Corrales *et al.* [7] sheds some light on the molecular pathways that dictate the asymmetric positioning of the pit and patterning of the myosin contraction. Furthermore, the patterning of forces is not imprinted on specific cells. Instead, cells approaching the pit during invagination may be dynamically assigned apicomedial contraction. Therefore, although one could improve the mechanical modeling by prescribing an asymmetric placode, a comprehensive solution may require resolving the first limitation noted above by incorporating the signaling proteins into the mechanical model. Another geometric assumption is synchronized intercalation on the basal and apical surfaces, even though the polarized contraction and neighbor exchange prevail mostly on the apical surface [2]. Thus, the model does not exhibit interleaving of cells as observed *in vivo*.

Finally, cell intercalation is one aspect of *in vivo* invagination that our model does not capture well. Qualitatively, the model predicts that intercalation tends to promote placode invagination, and suggests an active mechanism for the T1 transition. Both are in agreement with *in vivo* observations [2]. But quantitatively, the model is only able to predict a small contribution to tissue deformation and invagination, much below that reported *in vivo* [2]. Because our vertex-based representation is purely elastic, and does not account for cortical remodeling that imparts a viscous component to the tissue's mechanics, the *in silico* placode lacks the fluidity of the real placode. A viscoelastic model may moderate the elastic resistance to cell rearrangement and allow the large number of intercalations and fluid-like tissue deformation seen *in vivo*. In such a model, we expect the three myosin pools to perform their respective roles in much the same way as predicted by the current model.

As 3D modeling of epithelial morphogenesis is relatively new and underdeveloped, such limitations and omissions are arguably justifiable in a first attempt at quantitative modeling of the invagination of the *Drosophila* salivary gland. But they do provide incentives for development of better and more realistic models in future work.

Acknowledgment: This project was supported by the National Science and Engineering Research Council of Canada (NSERC) through a Discovery Grant No. 2019-04162. We thank Katja Röper and Yara Sánchez-Corrales (Cambridge University) for stimulating discussions and for critiquing a draft of the paper, and Leah Keshet (University of British Columbia, Vancouver) and Tony Harris (University of Toronto) for comments and suggestions on various aspects of the project. This work was supported by the University of British Columbia Advanced Research Computing initiative through the use of the Sockeye high performance computing cluster.

References

[1] K. Röper, Anisotropy of Crumbs and aPKC drives myosin cable assembly during tube formation, Dev. Cell 23 (5) (2012) 939–953.

[2] Y. E. Sanchez-Corrales, G. B. Blanchard, K. Röper, Radially patterned cell behaviours during tube budding from an epithelium, eLife 7 (2018) 1–36.

[3] S. Chung, S. Kim, D. J. Andrew, Uncoupling apical constriction from tissue invagination, eLife 6 (2017) 1–25.

[4] M. M. Myat, D. J. Andrew, Organ shape in the *Drosophila* salivary gland is controlled by regulated, sequential internalization of the primordia, Development 127 (4) (2000) 679–691.

[5] M. M. Myat, D. J. Andrew, Fork head prevents apoptosis and promotes cell shape change during formation of the Drosophila salivary glands, Development 127 (19) (2000) 4217–4226.

[6] P. L. Bradley, D. J. Andrew, *ribbon* encodes a novel *btb/poz* protein required for directed cell migration in *Drosophila Melanogaster*, Development 128 (15) (2001) 3001–3015.

[7] Y. E. Sanchez-Corrales, G. Blanchard, K. Röper, Correct regionalisation of a tissue primordium is essential for coordinated morphogenesis, bioRxiv doi: 10.1101/2020.08.29.273219.

[8] A. M. Cheshire, B. E. Kerman, W. R. Zipfel, A. A. Spector, D. J. Andrew, Kinetic and mechanical analysis of live tube morphogenesis, Dev. Dyn. 237 (10) (2008) 2874–2888.

[9] A. J. Booth, G. B. Blanchard, R. J. Adams, K. Röper, A dynamic microtubule cytoskeleton directs medial actomyosin function during tube formation, Dev. Cell 29 (5) (2014) 562–576.

[10] G. B. Blanchard, S. Murugesu, R. J. Adams, A. Martinez-Arias, N. Gorfinkiel, Cytoskeletal dynamics and supracellular organisation of cell shape fluctuations during dorsal closure., Development 137 (16) (2010) 2743–52.

[11] A. C. Martin, M. Kaschube, E. F. Wieschaus, Pulsed contractions of an actin-myosin network drive apical constriction, Nature 457 (7228) (2009) 495–499.

[12] A. C. Martin, Pulsation and stabilization: Contractile forces that underlie morphogenesis, Dev. Biol. 341 (1) (2010) 114–125.

[13] M. Llimargas, J. Casanova, Apical constriction and invagination: A very self-reliant couple, Dev. Biol. 344 (1) (2010) 4 – 6.

[14] B. K. Chauhan, M. Lou, Y. Zheng, R. A. Lang, Balanced *Rac1* and *RhoA* activities regulate cell shape and drive invagination morphogenesis in epithelia, PNAS 108 (45) (2011) 18289–18294.

[15] J.-Y. Lee, R. M. Harland, Actomyosin contractility and microtubules drive apical constriction in *Xenopus* bottle cells, Dev. Biol. 311 (1) (2007) 40–52.

[16] A. C. Martin, B. Goldstein, Apical constriction: themes and variations on a cellular mechanism driving morphogenesis., Development 141 (10) (2014) 1987–1998.

[17] T. F. Plageman, B. K. Chauhan, C. Yang, F. Jaudon, X. Shang, Y. Zheng, M. Lou, A. Debant, J. D. Hildebrand, R. A. Lang, A *Trio-RhoA-Shroom3* pathway is required for apical constriction and epithelial invagination, Development 138 (23) (2011) 5177–5188.

[18] G. Odell, G. Oster, P. Alberch, B. Burnside, The mechanical basis of morphogenesis: I. epithelial folding and invagination, Dev. Biol. 85 (2) (1981) 446–462.

[19] O. Polyakov, B. He, M. Swan, J. W. Shaevitz, M. Kaschube, E. Wieschaus, Passive mechanical forces control cell-shape change during drosophila ventral furrow formation, Biophys. J. 107 (4) (2014) 998–1010.

[20] F. L. Wen, Y. C. Wang, T. Shibata, Epithelial folding driven by apical or basal-lateral modulation: geometric features, mechanical inference, and boundary effects, Biophys. J. 112 (12) (2017) 2683–2695.

[21] R. Fernandez-Gonzalez, S. de Matos Simões, J.-C. Röper, S. Eaton, J. A. Zallen, Myosin II dynamics are regulated by tension in intercalating cells, Dev. Cell 17 (5) (2009) 736–743.

[22] H. Lan, Q. Wang, R. Fernandez-Gonzalez, J. J. Feng, A biomechanical model for cell polarization and intercalation during *Drosophila* germband extension, Phys. Biol. 12 (5) (2015) 056011.

[23] L. C. Siang, R. Fernandez-Gonzalez, J. J. Feng, Modeling cell intercalation during *Drosophila* germband extension, Phys. Biol. 15 (6) (2018) 066008.

[24] D. P. Kiehart, C. G. Galbraith, K. A. Edwards, W. L. Rickoll, R. A. Montague, Multiple forces contribute to cell sheet morphogenesis for dorsal closure in Drosophila, J. Cell Biol. 149 (2) (2000) 471–490.

[25] J. Solon, A. Kaya-Çopur, J. Colombelli, D. Brunner, Pulsed forces timed by a ratchet-like mechanism drive directed tissue movement during dorsal closure, Cell 137 (7) (2009) 1331–1342.

[26] H. Honda, M. Tanemura, T. Nagai, A three-dimensional vertex dynamics cell model of space-filling polyhedra simulating cell behavior in a cell aggregate, J. Theor. Biol. 226 (4) (2004) 439–453.

[27] S. Okuda, Y. Inoue, M. Eiraku, Y. Sasai, T. Adachi, Reversible network reconnection model for simulating large deformation in dynamic tissue morphogenesis, Biomechanics and Modeling in Mechanobiology 12 (4) (2013) 627–644.

[28] C. Bielmeier, S. Alt, V. Weichselberger, M. La Fortezza, H. Harz, F. Jülicher, G. Salbreux, A. K. Classen, Interface Contractility between Differently Fated Cells Drives Cell Elimination and Cyst Formation, Current Biology 26 (5) (2016) 563–574.

[29] M. Misra, B. Audoly, I. G. Kevrekidis, S. Y. Shvartsman, Shape Transformations of Epithelial Shells, Biophys. J. 110 (7) (2016) 1670–1678.

[30] S. Alt, P. Ganguly, G. Salbreux, Vertex models: From cell mechanics to tissue morphogenesis, Phil. Trans. R. Soc. B 372 (1720) (2017) 20150520.

[31] M. Osterfield, X. X. Du, T. Schüpbach, E. Wieschaus, S. Y. Shvartsman, Three-dimensional epithelial morphogenesis in the developing *Drosophila* Egg, Dev. Cell 24 (4) (2013) 400–410.

[32] X. Du, M. Osterfield, S. Y. Shvartsman, Computational analysis of three-dimensional epithelial morphogenesis using vertex models, Phys. Biol. 12 (1) (2015) 019501.

[33] V. Conte, J. J. Muñoz, M. Miodownik, A 3D finite element model of ventral furrow invagination in the *Drosophila melanogaster* embryo, J. Mech. Behav. Biomed. Mater. 1 (2) (2008) 188 – 198.

[34] R. Allena, A. Mouronval, D. Aubry, Simulation of multiple morphogenetic movements in the Drosophila embryo by a single 3D finite element model, J. Mech. Behav. Biomed. Mater. 3 (4) (2010) 313–323.

[35] M. Rauzi, A. H. Brezavšček, P. Ziherl, M. Leptin, Physical models of mesoderm invagination in *Drosophila* embryo, Biophys. J. 105 (2013) 3–10.

[36] L. A. Davidson, M. A. R. Koehl, R. Keller, G. F. Oster, How do sea urchins invaginate? Using biomechanics to distinguish between mechanisms of primary invagination, Development 121 (1995) 2005–2018.

[37] C. Durney, T. Harris, J. Feng, Dynamics of PAR proteins explain the oscillation and ratcheting mechanisms in dorsal closure, Biophys. J. 115 (11) (2018) 2230–2241.

[38] R. Clément, B. Dehapiot, C. Collinet, T. Lecuit, P. F. Lenne, Viscoelastic dissipation stabilizes cell shape changes during tissue morphogenesis, Curr. Biol. 27 (2017) 3132–3142.e4.

[39] T. Brody, The interactive fly: gene networks, development and the internet, Trends Genet. 15 (8) (1990) 333–334.

[40] C. Sidor, T. J. Stevens, L. Jin, J. Boulanger, K. Röper, Rho-kinase planar polarization at tissue boundaries depends on phospho-regulation of membrane residence time, Dev. Cell 52 (3) (2020) 364 – 378.

[41] C. Zmurchok, D. Bhaskar, L. Edelstein-Keshet, Coupling mechanical tension and GTPase signaling to generate cell and tissue dynamics, Phys. Biol. 15 (4) (2018) 046004.

[42] R. Farhadifar, J. C. Röper, B. Aigouy, S. Eaton, F. Jülicher, The influence of cell mechanics, cell-cell interactions, and proliferation on epithelial packing, Curr. Biol. 17 (24) (2007) 2095–2104.

[43] A. G. Fletcher, J. M. Osborne, P. K. Maini, D. J. Gavaghan, Implementing vertex dynamics models of cell populations in biology within a consistent computational framework, Prog. Biophys. Mol. Biol. 113 (2) (2013) 299–326.

[44] A. Fletcher, M. Osterfield, R. Baker, S. Shvartsman, Vertex models of epithelial morphogenesis, Biophys. J. 106 (11) (2014) 2291–2304.

[45] N. Murisic, V. Hakim, I. G. Kevrekidis, S. Y. Shvartsman, B. Audoly, From discrete to continuum models of three-dimensional deformations in epithelial sheets, Biophys. J. 109 (1) (2015) 154–163.

[46] E. M. Purcell, Life at low Reynolds number, Am. J. Phys. 45 (1) (1977) 3–11.

[47] Q. Wang, J. J. Feng, L. M. Pismen, A cell-level biomechanical model of *Drosophila* dorsal closure, Biophys. J. 103 (11) (2012) 2265–2274.

[48] K. V. Iyer, R. Piscitello-Gómez, J. Paijmans, F. Jülicher, S. Eaton, Epithelial viscoelasticity is regulated by mechanosensitive E-cadherin turnover, Curr. Biol. 29 (2019) 578–591.e5.

[49] R. J. Tetley, G. B. Blanchard, A. G. Fletcher, R. J. Adams, B. Sanson, Unipolar distributions of junctional Myosin II identify cell stripe boundaries that drive cell intercalation throughout *Drosophila* axis extension, eLife 5 (2016) e12094.

[50] R. Fernandez-Gonzalez, J. A. Zallen, Oscillatory behaviors and hierarchical assembly of contractile structures in intercalating cells, Phys. Biol. 8 (4) (2011) 045005.

Supporting Material for “A three-dimensional vertex model for *Drosophila* salivary gland invagination”

Clinton H. Durney[1*] and James J. Feng[1,2†]

[1]Department of Mathematics, University of British Columbia, Vancouver, Canada
[2]Department of Chemical and Biomedical Engineering, University of British Columbia, Vancouver, Canada

S1 Eccentric Pit

The model in the main text uses a concentric setup with the pit at the center. In reality, the pit is located at the dorsal-posterior corner of the placode. We have carried out some preliminary explorations with the eccentric-pit setup. In the following, we describe some of the eccentric-pit results and explain how they have motivated our decision of adopting the concentric geometry in the main paper.

On the basis of experimental images [1], we construct the placode with eccentric pit as in Fig. S1. In comparison with the concentric setup of Fig. 2 in the main paper, we have 4 partial myosin arcs instead of the 2 complete arcs. The apicomedial myosin atop the pit cells and the peripheral actomyosin cable are the same as in the concentric setup. The myosin levels in the different pools and the timing of their onset are also the same. In particular, the apicomedial myosin on the pit cells and the innermost arc onsets at $t = 0$, followed by the 3 outer arcs at $t = 375$ s. The peripheral cable starts at $t = 3500$ s. In addition, we need to implement adhesion forces between the edge of the placode and the surrounding tissue. These are represented by the blue springs emanating from the four edges of the placode closest to the pit. The strength of the adhesion is represented by the linear spring constant k_{ad}, which may vary in space.

S1.1 No adhesion

In our first test case, we set the adhesion force to zero all around the edge of the placode. The invagination process is shown in Movie S1. The apical constriction in the pit causes a small dip at the start, accompanied by the upward curling of the basal faces of the cells at the near-side edges. The junctional arcs, once activated, align the cell edges into more or less straight boundaries between abutting rows of cells, and pull on the edge of the placode. Being incomplete, however, these arcs are unable to convert their contractile force effectively into a radial force toward the pit. This is the starkest difference from the concentric placode discussed in the main paper. The peripheral cable constricts the whole tissue and causes the edge cells to curl up. But because of the eccentric location of the pit, this constriction mainly moves the pit inward toward the center of the tissue, instead of feeding the placode cells into an invaginating pit. The final configuration, depicted in Fig. S2(a,d), features a broad and gentle depression over much of the placode, except for a sharp upturn near the pit. The center of the pit is not even the lowest point in the depression. This shape is far from the tube-like shape *in vivo* or the dome-like shape produced by the concentric placode in the main paper.

---

[*] Current address: John Innes Centre, Norwich Research Park, Norwich, United Kingdom
[†] james.feng@ubc.ca

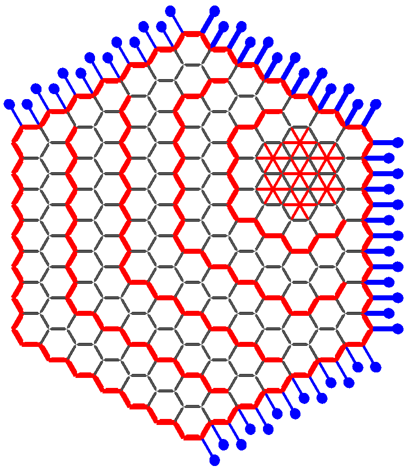

Figure S1: Geometric setup for the placode with an eccentric pit. The red lines mark edges and spokes carrying contractile myosin force. The blue lines are linear springs representing adhesive bonds to the surrounding tissue. Their resting length equals the undeformed cell edge length, and their outer end is fixed in space. The spring constant may be set to zero (no adhesion as in Sec. S1.1) or spatially nonuniform values (Sec. S1.2).

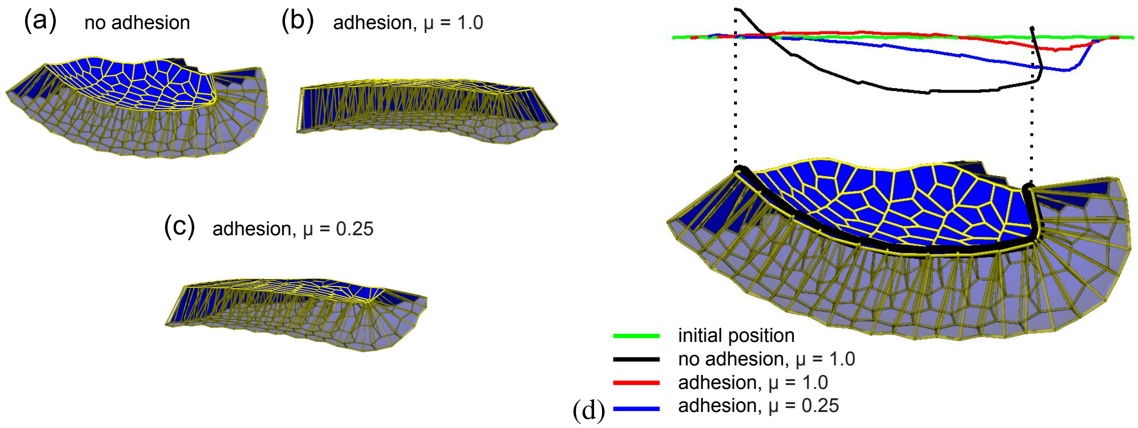

Figure S2: Comparison of the final configuration of three eccentric placodes, taken at $t = 20000$ s. (a) Cross-sectional view of the placode without adhesion; (b) with adhesion and the cell edges at the baseline stiffness ($\mu = 1$ nN/μm); (c) with adhesion and a reduced edge stiffness ($\mu = 0.25$ nN/μm); (d) contours of the apical surface in the three cases, the no-adhesion case serving as an example to illustrate the geometric correspondence. The horizontal green line marks the common initial position for all three cases.

The lesson from the above test is that the placode fails to invaginate in the absence of adhesion with surrounding tissues. Without "anchoring" on the surrounding tissue, the junction myosin arcs cannot effectively push the cells toward the pit to feed the invagination. The peripheral cable causes an overall constriction that moves the pit inward toward the center of the placode and curls up the near-side edge, without deepening the invagination at the pit.

S1.2 Spatially nonuniform adhesion

The foregoing observations suggest that adhesion is needed, especially on the near-side edge, to anchoring the placode and prevent the pit from moving and tilting. Thus we deploy strong linear springs with elastic constant $k_{ad} = 100\,\mathrm{nN}\,\mathrm{\mu m}^{-1}$ on the near-side edges closest to the pit (thick blue lines in Fig. S1) and weaker ones with $k_{sd} = 10\ \mathrm{nN}\,\mathrm{\mu m}^{-1}$ on the two side edges (thin blue lines). No adhesion is applied to the two far-side edges. The invagination process is shown in Movie S2, with the final configuration in Fig. S2(b,d).

The most obvious benefit of the adhesion is to prevent the pit from moving inward and tilting upward. Thus, the center of the pit remains the deepest point across the placode (Fig. S2d). The tissue shape has greater regularity, as the asymmetric curling of the basal surface is largely suppressed. However, the expected benefit of deeper invagination has not materialized. In fact, the adhesion keeps the tissue from overall bending, with the result of a much shallower depression at the pit. The reason is that the junctional arcs and the peripheral cable are still unable to herd the cells toward the pit. Based on the observations so far, we hypothesize that successful invagination *in vivo* requires two factors acting in concert: strong adhesion on the near-side edge together with effective cell movement and tissue deformation driven by the junctional and peripheral myosin.

In particular, the myosin constriction must drive the cells from the far side of the placode over long distances into the pit, considering the eccentric position of the pit. In fact, many of the far-side cells will need to execute an extraordinary movement of first going down the inner side of the lumen (left side of the pit in the depiction of Fig. S2d), then rounding the tip of the tube that extends downward continually, and finally climbing back up on the opposite side of the lumen. This is indeed a stringent requirement on cell movement and tissue deformation. The adhesion with far-side tissues, which has not been considered here, will raise the requirement even further.

As discussed in the main text, Sec. 3.2.2, the junctional myosin forces in our model cannot generate sufficient numbers of intercalations to effectively drive the tissue toward the pit. The main reason is not the magnitude of the myosin forces, but the unrealistically stiff resistance of the model placode in its vertex-based, purely elastic representation. In reality, cortical remodeling happens at a rapid rate relative to the time scale of the invagination [2], and this affords the tissue much greater fluidity that can accommodate intercalations and effect convergence along the azimuthal direction and radial extension toward the pit [1, 3].

Instead of making fundamental changes to the vertex model, to add viscoelasticity for example [4], we have tested softening the placode by reducing the elastic constant μ of the edges and spokes. A simulation where μ is reduced to 1/4 of its baseline value is shown in Movie S3, with the final configuration depicted in Fig. S2(c,d). The invagination goes further in this case, with more marked movement of the placode from the far side toward the pit. Even though the final configuration is still far from the expected shape, this test supports our hypothesis that in an eccentric pit, one needs strong adhesion forces coupled with effective displacement and deformation of the placode tissue.

The above tests suggest to us that to produce proper invagination in an eccentric placode, a purely elastic vertex-based model is probably inadequate. Greater placode fluidity and numerous cell intercalations are needed. It is the recognition of the inadequacies of the current vertex-based model that has motivated us to adopt a concentric setup in the main paper. This setup facilitates the centripetal movement of the cells and alleviates the difficulties related to adhesion and tissue fluidity to some extent. Thus, the model can help us explore the roles of the different myosin pools in the invagination process, while leaving out several complexities in the *in vivo* process, including those noted in the above and others discussed at the end of the main paper (Sec. 4). All subsequent results and discussions are based on the concentric model.

S2 Calculation of Forces

S2.1 Forces due to pressure

The first term of Eq. (1) of the main paper represents volume conservation of an individual cell,

$$E_n = \frac{\alpha}{2}(V_n - V_0)^2. \tag{S1}$$

By differentiating E_n with respect to cell volume, V_n, we obtain the pressure of cell n [5]:

$$P_n = -\alpha(V_n - V_0). \tag{S2}$$

Note that this is actually the pressure difference with respect to the ambient pressure, and thus vanishes in the undeformed cell. To convert the pressure in a cell into a force on each of its nodes, we first compute the pressure force on each of the triangular areal elements on its apical and basal faces, and then distribute the force equally among the three vertices of the triangle. Thus, each node receives this force:

$$\mathbf{F}_P = \frac{1}{3}P\mathbf{A}, \tag{S3}$$

where $\mathbf{A}$ is the vectorial area of the triangle, pointing in the outward normal direction of the triangle (see an illustration in Fig. 1 of the main paper). Thus, the pressure pushes on the given areal element in the direction of the outward normal vector.

The lateral faces of a cell lack a central node, and we need to triangulate them for distributing the pressure force. We first calculate the centroid of the 4 vertices of a lateral face, at each time step:

$$\mathbf{x}_c = \frac{1}{4}\sum_{i=1}^{4}\mathbf{x}_i. \tag{S4}$$

This now gives a triangulation of a lateral face (see Fig. 1 of the main paper). For each triangle, we compute its area and normal vector as we do for the triangular areal elements of the apical and basal surfaces. Because the newly computed centroid is not a node, and does not carry force in computing the evolution of the cell, we assign the pressure force on each triangle to only the 2 nodes on the apical or basal surface:

$$\mathbf{F}_P = \frac{1}{2}P\mathbf{A}. \tag{S5}$$

In the end, the pressure force on each node is the vectorial sum of contributions from all the lateral, apical and basal triangles that share the node, including those from the neighboring cells.

S2.2 Elastic forces

The second term of Eq. (1) represents elastic energy on the cell edges (on the apical, basal and lateral faces) and spokes (on the apical and basal faces only). It gives rise to linearly elastic "spring forces" on the edges and spokes. The calculation of these forces is straightforward, and follows that of previous vertex models [6, 7].

S2.3 Force due to bending

The third and final term of Eq. (1) represents a bending energy that penalizes out of plane deformations of the tissue. The bending force on a vertex is determined from the relative orientation of a pair of triangles that share a common edge. As Fig. 1 shows, the bending between triangles a and b will produce a force on each of the vertices of the two triangles serving to align the normal vectors $\hat{\mathbf{A}}_a$ and $\hat{\mathbf{A}}_b$. We follow the formulation of Du et al. [8] and Murisic et al. [9] in evaluating such nodal forces.

Before deriving the force for each node, we first establish the derivative of the vectorial area of an apical or basal triangular face, $\mathbf{A}_a$, with respect to node position, $\mathbf{x}$,

$$\frac{\partial \mathbf{A}_a}{\partial \mathbf{x}} = \frac{1}{A_a} \sum_{k=1}^{3} A_a^k \frac{\partial A_a^k}{\partial \mathbf{x}}, \tag{S6}$$

and the derivative of the k^{th} component of $\mathbf{A}_a$,

$$\frac{\partial A_a^k}{\partial \mathbf{x}} = \frac{1}{2}(\mathbf{x}_{i-1} - \mathbf{x}_{i+1}) \times \mathbf{e}^k, \tag{S7}$$

where $\mathbf{x}_{i-1}$ and $\mathbf{x}_{i+1}$ indicate the neighboring nodes to $\mathbf{x}$ and $\mathbf{e}^k$ represent the standard basis vectors in $\mathbb{R}^3$.

We can now calculate the force on node $\mathbf{x}$ due to the bending energy of triangular area elements a and b:

$$\begin{aligned}
\mathbf{F}_{\mathbf{x}\langle ab\rangle} &= \rho \frac{\partial}{\partial \mathbf{x}}(-\mathbf{A}_a \cdot \mathbf{A}_b) = \rho \frac{\partial}{\partial \mathbf{x}} \left(\frac{1}{A_a A_b} \sum_{k=1}^{3} A_a^k A_b^k \right) \\
&= \rho \left(\frac{1}{A_a A_b} \right) \left(\sum_{k=1}^{3} A_b^k \frac{\partial}{\partial \mathbf{x}} A_a^k + \sum_{k=1}^{3} A_a^k \frac{\partial}{\partial \mathbf{x}} A_b^k \right) \\
&\quad + \rho \frac{-\sum_{k=1}^{3} A_a^k A_b^k}{(A_a A_b)^2} \left(\frac{A_a}{A_b} \sum_{k=1}^{3} A_b^k \frac{\partial A_b^k}{\partial \mathbf{x}} + \frac{A_b}{A_a} \sum_{k=1}^{3} A_a^k \frac{\partial A_a^k}{\partial \mathbf{x}} \right).
\end{aligned} \tag{S8}$$

As a node may belong to multiple triangular area elements, the total bending force on it is the sum of the force $\mathbf{F}_{\mathbf{x}\langle ab\rangle}$ over all pairs of area elements $(\mathbf{A}_a, \mathbf{A}_b)$ associated with node $\mathbf{x}$.

S2.4 Active myosin forces

All edges and spokes are passively elastic, as described above. But *apical* edges and *apical* spokes are special in that they may also carry myosin, and thus an active contractile force due to myosin:

$$\mathbf{F}_{ij}^{\text{myo}} = \beta m_{ij} \frac{\mathbf{x}_j - \mathbf{x}_i}{|\mathbf{x}_j - \mathbf{x}_i|}, \tag{S9}$$

where β is the force per myosin motor and m_{ij} is the number of myosin motors on the edge connecting nodes i and j. Note that under this formulation, lateral and basal edges remain strictly passively elastic throughout the simulation ($m_{ij} = 0$ for all t) and their dynamics is fully governed by Eq. (1).

Unlike in previous vertex models [6, 7], we do not account for the kinetics of myosin activation and deactivation in this model. Rather, the myosin force is assumed to onset abruptly on chosen edges and spokes, according to the designation of the myosin pools in Sec. 2.1 of the main text, and then to stay at a constant value for the duration of the simulation. The only exception is if the edge contracts to a point during T1 transition. When the point extends into a new edge in the orthogonal direction, it carries no myosin for the remainder of the simulation. More details about the T1 transition are given below in Sec. S8. The magnitude of the myosin force F^{myo} on different edges and spokes will be discussed below in Sec. S3.4.

S3 Model Parameters

We have summarized all model parameters in Table S1. Whenever possible, we have estimated parameters from the literature. If values are not available for *Drosophila*, we have adopted data for other organisms if available. If no reliable information is present, we choose values to produce desirable behavior of the salivary gland placode. The evaluation of several key parameters are elaborated below.

Table S1: Values of the parameters used in the model and their sources where available.

Parameter types	Meaning	Symbol	Value	Sources
Geometric	Number of cells in placode	n	127 cells	[1, 10, 11]
	Apical edge and spoke rest length	l_0	3.6 μm	[1]
	Basal edge and spoke rest length	l_0	3.6 μm	[1]
	Lateral edge rest length	L_0	13.6 μm	[1]
	Intercalation threshold length	l_{min}	0.1 μm	This work
Mechanical	Edge and spoke elastic constant	μ	1.0 nN μm^{-1}	[12, 13]
	Pressure constant of the cell	α	0.046 nN μm^{-5}	[14]
	Bending energy	ρ	3.0 nN μm	This work, [15]
	Force per myosin motor	β	10^{-3} nN/motor	[16]
	Viscous friction factor	η	100.0 nN s μm^{-1}	[13, 17, 18]
Apicomedial myosin	Onset time	t	0 s	[1, 19]
	Contractile force per spoke	F^{myo}	0.54 nN	[16, 20, 21]
Inner myosin arc	Onset time	t	0 s	[1, 19]
	Contractile force per edge	F^{myo}	0.75 nN	[16, 19–21]
Outer myosin arc	Onset time	t	375 s	[1]
	Contractile force per edge	F^{myo}	0.75 nN	[16, 19–21]
Intercalating edges	Onset time	t	375 s	[1]
	Contractile force per edge	F^{myo}	1.0 nN	This work
Supracellular actomyosin cable	Onset time	t	3500 s	[1, 22, 23]
	Contractile force per edge	F^{myo}	0.75 nN	[16, 19–21]

S3.1 Elastic constant of the cell edges and spokes

As the undeformed placode comprises a collection of columnar cells, and each cell is represented by elastic edges (or springs) connecting the vertices, we seek to evaluate the elastic constant μ of these edges from the overall Young's modulus E of the placode under uniaxial compression. In the vertex model, this compression only shortens the lateral edges, not those on the apical and basal faces. We will estimate the spring constant μ for the lateral edges, and assign the same value to the apical and basal edges and spokes.

Take the apical area of the placode to be A, and the total number of lateral edges to be n. When a force F is applied to compress the placode, the resulting strain $\epsilon = (F/A)/E$ is also the strain $\delta L/L_0$ suffered by each lateral edge, L_0 being the undeformed thickness of the placode. Thus, we can relate the overall modulus E to the spring constant μ for each lateral edge:

$$E = \frac{F}{A}\frac{L_0}{\delta L} = \frac{F}{\delta L}\frac{L_0}{A} = \frac{n\mu L_0}{A}.$$

Lacking specific data for the modulus of *Drosophila* salivary gland placode, we choose to adopt the modulus of *S. purpuratus* embryo, with E reported in the range of $600 \sim 2000\ \text{Pa} = 0.6 \sim 2.0\ \text{nN}\,\mu\text{m}^{-2}$ [13]. The number of cells in the placode ranges from 75 to 150 [1, 10, 11]. Assuming 100 cells with a hexagonal apical surface of edge length $l_0 = 3.6$ μm (see Table S1), we estimate the total cross-sectional area to be $A = 3000\ \mu\text{m}^2$ [19]. The lateral length L_0 is taken to be 13.6 μm (Table S1). With the placodal cells represented by hexagons, an individual cell has 6 lateral springs, some of which are shared among neighboring cells. For the model placode used here, the total number of lateral edges is $n = 240$.

Using the above parameters, we estimate the spring constant μ to be in the range of $0.55 \sim 1.84\,\mathrm{nN\,\mu m^{-1}}$, and take $\mu = 1\ \mathrm{nN\,\mu m^{-1}}$ to be the baseline value in Table S1. This value happens to coincide with that for amnioserosa cell edges during *Drosophila* dorsal closure [12].

S3.2 Pressure coefficient of the cell

Equation (S2) gives the pressure inside each cell: $P = -\alpha(V - V_0)$. The coefficient α can be estimated from the bulk modulus K of the cell, defined by

$$K = -V\frac{dP}{dV} \approx -V\frac{P}{V - V_0} = \alpha V,$$

where the pressure of the undeformed cell is set to zero in our convention, as noted below Eq. (S2). Thus, we obtain

$$\alpha = \frac{K}{V}.$$

We have found little data on the bulk modulus of biological cells. Meanwhile, the Young's modulus E has been measured for various epithelial cells in the literature [14, 24]. For *Drosophila* epithelial cells, for example, E was estimated to be $1.8\ \mathrm{kPa} = 1.8\ \mathrm{nN\,\mu m^{-2}}$ [14]. Assuming a Poisson ratio of $\nu = 0.4$ based on the typical range of soft materials [25, 26], we can calculate the bulk modulus K for epithelial cells using the relation

$$K = \frac{E}{3(1 - 2\nu)}.$$

This yields an estimated bulk modulus of $K = 3.0\ \mathrm{nN\,\mu m^{-2}}$. Using the cell volume $V = 65\ \mathrm{\mu m^3}$, we obtain the pressure coefficient $\alpha = 0.046\ \mathrm{nN\,\mu m^{-5}}$.

S3.3 Bending energy

In the literature, a wide range of values have been reported for the epithelial bending energy coefficient ρ, from 1 to $100\ \mathrm{nN\,\mu m}$ [15]. As our baseline value, we choose $\rho = 3\ \mathrm{nN\,\mu m}$ to strike a balance between two opposing tendencies. If ρ is too small (e.g. $1\ \mathrm{nN\,\mu m}$), the placode becomes susceptible to local distortions under radial compression. Certain nodes jut upward or downward out of the apical plane to form short-wavelength "wrinkles", and consequently invagination fails. Conversely, if ρ is too high (e.g. $10\ \mathrm{nN\,\mu m}$), only a shallow pit can be formed under reasonable myosin constriction, and again invagination fails. Based on a series of numerical experiments, detailed below in Section S4, we have chosen the baseline value of $\rho = 3\ \mathrm{nN\,\mu m}$.

S3.4 Active forces due to myosin contraction

In reality, the interaction of myosin motors with actin filaments involves an intricate power stroke based on ATP hydrolysis. There is also a load-dependent feedback mechanism [27–29]. Unlike in previous vertex models [6, 7], we do not account for the kinetics of myosin activation and deactivation in this model. Rather, we impose a contractile force F^{myo} that onsets abruptly on chosen cell edges and spokes, according to the designation of the myosin pools in Sec. 2.1 of the main text. The magnitude of this force may differ between the different pools, and will be estimated below.

With each myosin motor generating on the order of 10^{-3} nN of force [16], estimating F^{myo} on a given edge or spoke amounts to estimating the number of myosin motors on it. The density of myosin on actin filaments fall in a wide range, of which we take 50 motors per μm to be a reasonable estimate [20]. The number of actin filaments in the cortex of the *Drosophila* placode cells has not been reported, and we can make an estimation from other cell types. For example, in melanoma and fibroblast cells, actin filaments accumulate in bundles of approximately 10 actin filaments [21]. Assuming a similar number for each spoke of the placode cell, we take 540 myosin motors per spoke as a reasonable estimate. This leads to the estimation of $F^{\text{myo}} = 0.54$ nN per spoke as given in Table S1.

To estimate the contractile force of the junctional myosin, we use as a rough guideline the observation that during the late stage of "deep invagination", the junctional myosin intensity is roughly 3.72 times that of apicomedial myosin [19]. However, it is unclear whether the peripheral actomyosin cable was included in the junctional myosin, and whether the ratio was between the total amounts of junctional and apicomedial myosin over the placode or the average of such a ratio for each individual cell. In our model setting, apicomedial myosin only exists on the seven cells in the pit. Thus, we can only take the ratio between the total amounts of junctional and apicomedial myosin. As the baseline, we have chosen 750 myosin motors on each edge that carries junctional myosin, corresponding to $F^{\text{myo}} = 0.75$ nN. The same force is used on the peripheral edges that form the actomyosin cable. Thus, the junctional/apicomedial myosin ratio will be 2.78 if the peripheral cable is excluded, and 5.36 if it is included, the two values straddling the *in vivo* ratio of 3.72. To alleviate concerns about this uncertainty, we have carried out a parametric study of raising the junctional myosin by up to 40%. This produces only minor changes in the invagination depth. Details are given in Sec. S4 below.

Finally, as noted in the main text, we impose a greater force on an edge slated for intercalation. Such an edge carries 1000 myosin motors and a force of $F^{\text{myo}} = 1$ nN to ensure strong contraction of the edge that will trigger an intercalation event (more details in Sec. S8 below).

S3.5 Viscous friction factor

As stated in the main text, the parameter η represents the combined effect of several frictional forces. Its value has been estimated in different contexts before [12, 13, 17, 18]. Davidson et al. [13] give a range for the *S. purpuratus* embryo: $\eta = 17 \sim 76\ \mathrm{nN\,s\,\mu m^{-1}}$. A larger value of $\eta = 100\ \mathrm{nN\,s\,\mu m^{-1}}$ is used in modelling the amnioserosa during *Drosophila* dorsal closure [6, 7, 12]. For this study, we take the value of $\eta = 100\ \mathrm{nN\,s\,\mu m^{-1}}$. Note that the viscous coefficient only affects the speed of nodal movement. It defines a time scale for the process, but does not influence the sequence of morphogenetic events nor the final morphology.

S4 Model Sensitivity to Key Parameters

To address uncertainties in parameter evaluation, we have performed a sensitivity analysis by varying each of the mechanical parameters of the energy functional in Eq. (1) of the main text: the pressure constant α, the bending energy coefficient ρ and the elastic constant of the edges and spokes μ. We have also varied the junctional myosin force F^{myo} on the myosin arcs. The results, depicted in Fig. S3, show that the qualitative features of the model predictions are robust around the baseline values. Quantitatively, the invagination depth varies little as α, ρ or F^{myo} changes, but is more sensitive to the elastic constant μ.

For the mechanical parameters α, μ and ρ, we cover a range of approximately 1/4 to twice the baseline value. The pressure coefficient α and the bending energy coefficient ρ have minor effects on the invagination depth. When α is varied within the range tested, the invaginated depth changes by 0.15% (Fig. S3a). The lack of a strong α effect suggests that volume conservation is not a significant player in the invagination process in our model. With increasing resistance to bending, the invagination depth decreases monotonically, as can be expected, but only by 2.15% in the ρ range tested (Fig. S3b). However, the apparent insensitivity to ρ belies an important role of the bending resistance.

Figure S4 compares the cross-sectional view of the placode at roughly the midpoint of the invagination

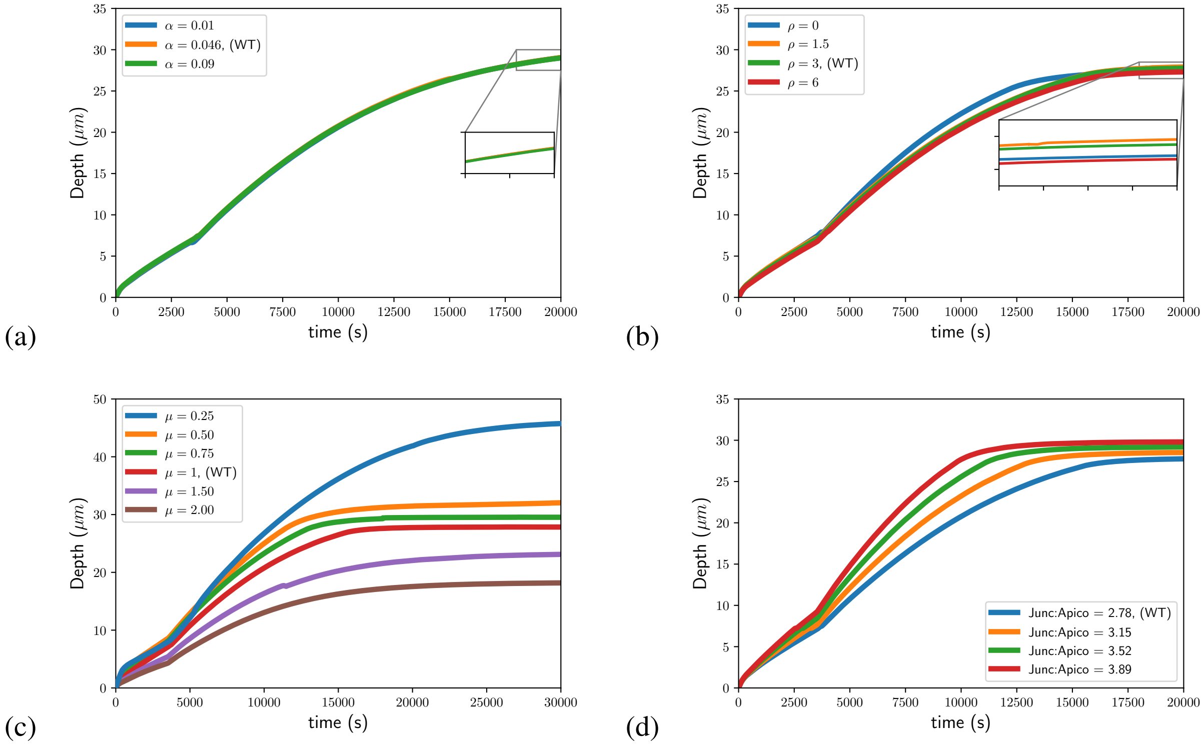

Figure S3: Sensitivity of invagination depth to key model parameters: (a) the pressure coefficient α, (b) the bending energy coefficient ρ, (c) the edge elastic constant μ, and (d) the amount of myosin on the junctional myosin arcs, represented by the ratio between the total amount of junctional myosin (excluding the peripheral cable) and the total amount of apicomedial myosin in the pit cells. For α, μ and ρ, the units are the same as in Table S1 and have been omitted from the legends. The model shows robust invagination depth around the baseline parameters, which are used in the *in silico* wild type (WT).

($t = 10000$ s) for 4 different values of ρ. If the bending resistance is absent or low ($\rho = 0$ or $1.5\ \mathrm{nN\,\mu m}$), the central nodes on the apical surfaces tend to buckle out of the plane under compression, thus producing unrealistic undulations in the placode (Fig. S4a,b). Greater resistance to bending eliminates the short-wave buckling in Fig. S4(c,d). Thus, the bending elasticity helps maintain the geometric integrity of the apical surface of the placode. Prior 3D vertex models usually do not posit an explicit bending resistance [30]. They rely instead on edge, surface and volume elasticity of the system for an effective resistance to bending. Such models typically do not employ apical spokes or central nodes, and are thus less susceptible to short-wave buckling. To our model, the representation of apicomedial myosin is essential, and consequently so is the bending elasticity.

Among the three mechanical parameters α, μ and ρ, the edge elasticity μ has the strongest effect on the invagination depth. Given the same myosin contractile force, a larger elastic constant means a greater resistance to edge deformation and consequently a shallower invagination. As μ increases from 1/4 to twice the baseline value, the steady-state invagination depth decreases by a factor of about 3 (Fig. S3c). Interestingly, the exercise of reducing μ can be likened to giving the vertex-based placode more "fluidity", making it softer and more liable to deformation and cell intercalation. For the softest $\mu = 0.25\ \mathrm{nN\,\mu m^{-1}}$, we observe spontaneous intercalations in the pit after it has invaginated into the nadir of the tube, and a final morphology with a narrower lumen and a more elongated shape (Fig. S5). The simulation can be seen in Movie S6, with the moments of intercalation noted in the caption. As noted in the main text, the

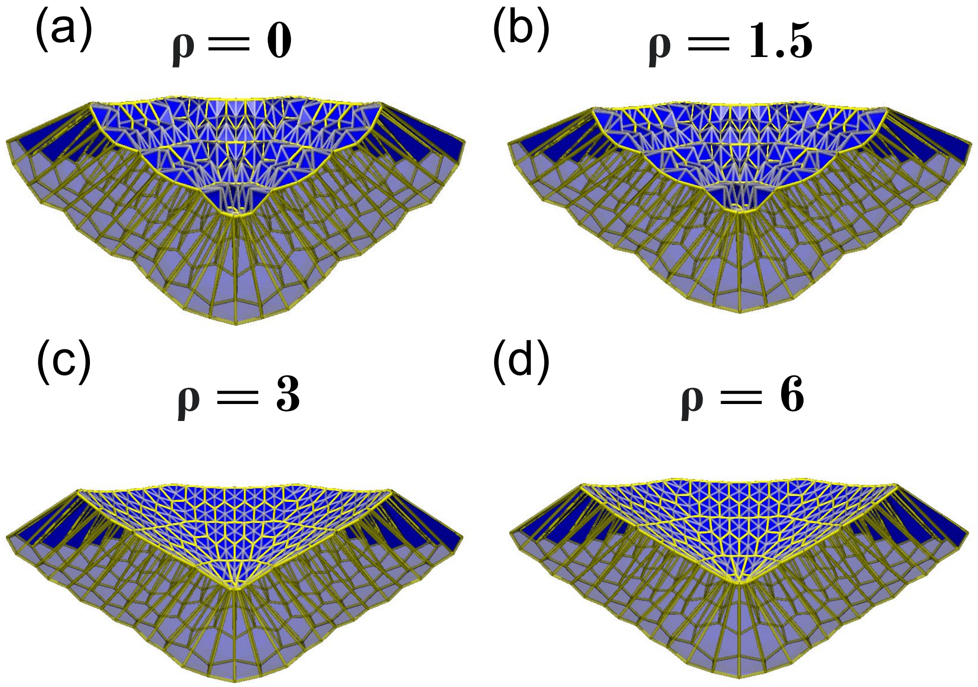

Figure S4: Cross-sectional snapshots at $t = 10000$ s for different values of the bending coefficient: (a) $\rho = 0$, (b) $\rho = 1.5$ nN μm, (c) $\rho = 3$ nN μm, and (d) $\rho = 6$ nN μm. The cell boundaries are colored yellow and the spokes on the apical faces are shown in light grey. Without adequate resistance to bending ($\rho \leq 1.5$ nN μm), buckling occurs on individual apical cell faces. At higher values of $\rho = 3$ and 6 nN μm, such buckling is suppressed.

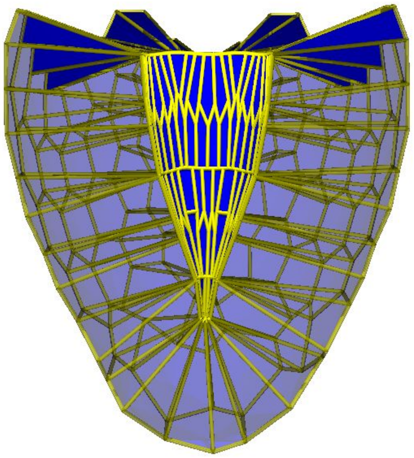

Figure S5: Cross-sectional view of the steady-state configuration of the concentric placode when the edge and spoke elastic constant is reduced to $\mu = 0.25$ nN/μm from its baseline value of $\mu = 1$ nN/μm.

model allows far fewer intercalations than *in vivo*, and we have attributed this failing to neglecting viscous aspect of the tissue associated with cell remodeling. The soft-μ test provides circumferential support for this argument.

Lastly, Fig. S3(d) explores the effect of increasing the myosin intensity on the junctional myosin arcs. This is motivated by the uncertainty in estimating the junctional myosin level from experimentally reported junctional-to-apicomedial myosin ratios (see Sec. S3.4). The baseline value of 750 myosin motors per junctional edges produces a junctional-to-apicomedial myosin ratio of 2.78, below the ratio of 3.72 reported in [19]. Therefore, we have increased the junctional edge to 850, 950 and 1050 myosin motors per edge, corresponding to a ratio of 3.15, 3.52 and 3.89, respectively. These three cases see only marginal increase in invaginated depth, within 7.5% of the WT placode. Thus, the uncertainty in estimating junctional myosin has had at most a minor effect on the model predictions.

S5 Numerical Scheme

The numerical computation for the vertex model consists in determining the trajectory of each vertex $\mathbf{x}_i(t)$ by solving a system of ordinary differential equations. This has been programmed in the Python programming language with NumPy and SciPy libraries. The numerical algorithm consists of the following steps:

Step 0: Initialize the stress-free initial configuration of the tissue.

Step 1: Calculate the volume of each cell of the tissue by finding the convex hull of the collection of nodes that make up a single cell using `scipy.spatial.convexhull`.

Step 2: If required, update the myosin concentration (i.e., contractile force) on a given edge. This is done only on the time step when the myosin gets activated on the edge.

Step 3: Calculate the elastic forces acting on each node (i) of the system. This is done by finding all the neighboring nodes (j) and summing up the elastic spring forces based on the Euclidean distance l_{ij} between the connected nodes. Thus, the total force acting on node i is given by

$$\mathbf{F}_i = \sum_j \mu(l_{ij} - l_0)\frac{\mathbf{x}_j - \mathbf{x}_i}{|\mathbf{x}_j - \mathbf{x}_i|}.$$

Step 4: Calculate the pressure force on each node by iterating through all cells sharing the node and calculating the force on it according to Sec. S2.1 by using the volume calculated in Step 1.

Step 5: Calculate the bending force on each node by iterating over each triangle pair (a, b) of the system and calculating the force according to Sec. S2.3.

Step 6: Update the position of each node by solving Eq. (3), rewritten here:

$$\eta\frac{d\mathbf{x}_i}{dt} = \mathbf{F}_i^{\text{con}} + \mathbf{F}_{ij}^{\text{myo}},$$

where η is the viscous coefficient and the right-hand-side is the vectorial sum of all forces acting on the node found in Steps (2)–(5). The equation is solved numerically for each vertex using the forward Euler scheme with sufficiently small time step Δt.

Step 7: Check for cellular rearrangments due to cellular intercalation, with details given in Sec. S8.

Step 8: Advance time by the time step Δt and repeat steps (1)–(7).

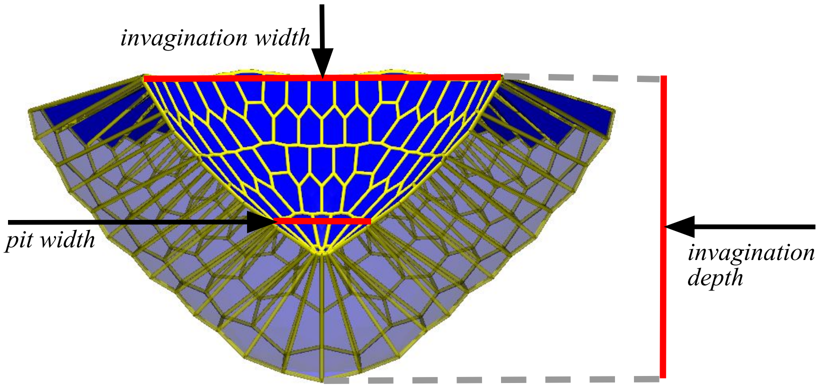

Figure S6: Schematic for the definitions of the depth and width of the invagination and the pit width.

S6 Geometric Dimensions of the Invagination

Typically, the central cell of the concentric placode ends up at the tip of the budding tube and we use its position to define the depth of invagination (Fig. S6). Specifically, we calculate the depth as the average of the vertical coordinate z_i of the 6 peripheral nodes on the basal face of the central cell:

$$d = \frac{1}{6}\sum_{i=1}^{6} z_i, \tag{S10}$$

where z_i has its origin on the horizontal plane that averages the position of the basal nodes at the “lip” of the tube.

The width w of the salivary gland is defined as the maximal Euclidean distance between basal nodes on the periphery of the placode:

$$w = \max\|\mathbf{x}_i - \mathbf{x}_j\|_2 \tag{S11}$$

where $\mathbf{x}_i$ and $\mathbf{x}_j$ run over all basal nodes of the boundary. The aspect ratio is simply d/w.

Finally, we define the width of the pit as the maximal Euclidean distance between apical nodes associated with the inner myosin arc. This is used in Fig. 10(a) of the main paper for comparison with the experiments of Chung et al. [11].

S7 Additional Mutant Studies

The discussion of *in silico* mutants in the main text focuses on a series of mutants that retain only one of the three myosin pools, the apicomedial myosin in the pit, the junctional myosin arcs, and the actomyosin cable around the periphery of the placode. In addition, we have studied another series of mutants with one of the three pools deactivated, and the other two pools intact. These results are presented here in Fig. S7, and shed additional light on the distinct roles played by each myosin pool.

The “absent apicomedial” mutant is the least impaired in terms of generating invagination depth; it attains about 98% of the final depth of the WT (Fig. S7a). However, its initial rate of invagination is the lowest among all the mutants, and the depth lags behind that of the WT by some 2500 s. This leads to two interesting observations. First, the apicomedial contraction on the pit cells contributes little directly to the depth of invagination. This is because of the relatively small number of pit cells covering a limited spatial expanse. Second, the apicomedial myosin nonetheless plays a distinct role initially. Once activated,

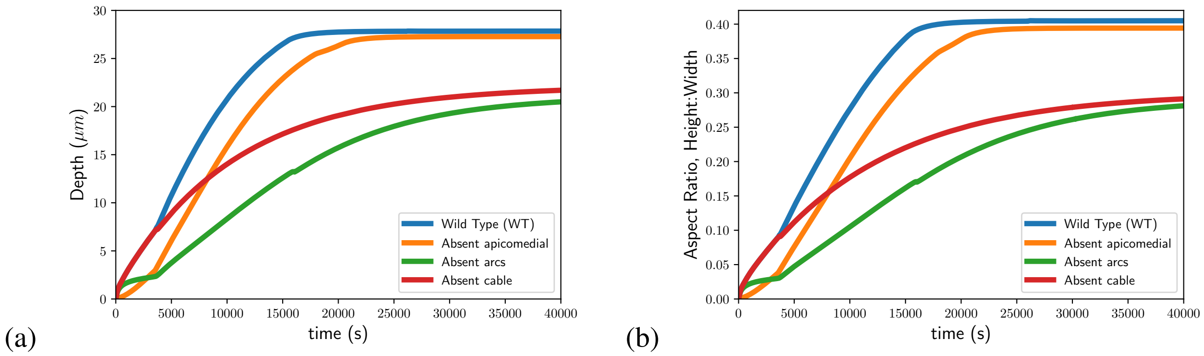

Figure S7: Comparison among a series of *in silico* mutants with one of the three myosin pools deactivated and the other two intact. For example, the "absent apicomedial" mutant has the apicomedial myosin atop the pit cells suppressed, but the junctional myosin arcs and the peripheral actomyosin cable fully functional. (a) The invagination depth. (b) The aspect ratio of the final shape.

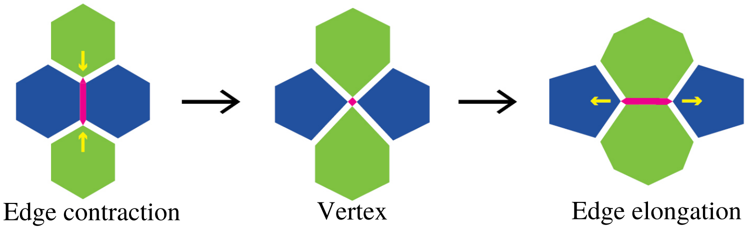

Figure S8: Schematic of cellular intercalation or T1 transition. During a T1 transition, an edge contracts into a vertex. A new edge then expands in the perpendicular direction. Image adapted from [31] under licence CC BY 3.0.

it produces a small invagination at the pit, and that initial out-of-plane deformation allows the outer myosin arcs to be more effective in converting their constrictive forces into depth of invagination. The absence of this initial deformation explains the delay experienced by the "absent apicomedial" mutant.

The "absent cable" mutant coincides with the WT until the peripheral cable onsets at $t = 3500$ s. It eventually achieves an invagination depth that is 22% below that of the WT (Fig. S7a). Thus, the cable makes a sizable contribution to the final invaginated depth. Besides, missing the peripheral cable also results in a wider opening in the end, such that the absent-cable mutant achieves a low aspect ratio of 0.29, a 28% drop relative to the WT (aspect ratio = 0.40; see Fig. S7b), a greater percentage drop than that in the depth. So the cable helps both to narrow the opening and to deepen the invagination, thus producing a greater aspect ratio. These effects of the peripheral cable have been noted in the main paper. Finally, the "absent arcs" mutant has the slowest and shallowest invagination, consistent with the observations in the main paper that the junctional myosin arcs are the most important drivers of invagination.

S8 Cellular Intercalation

To implement cellular intercalation, we follow a similar procedure to previous vertex based modeling [8, 31, 32]. A T1 transition is triggered whenever the length of an edge falls below a threshold value, l_{min} (Fig. S8). Then it is replaced by a new edge of the same length l_{min} oriented in the orthogonal direction. In numerical implementation, we examine the length of all edges. If the length of an edge between nodes

i and j is below the threshold, $|\mathbf{x}_i - \mathbf{x}_j| < l_{\text{min}}$, we contract the edge to a single vertex at its geometric center (Fig. S8 first and second panel), and then elongate a new edge towards the central nodes of the two cells oriented orthogonally to the contracted edge to length l_{min} (Fig. S8 last panel). As in previous models for intercalation [31, 33], we assume that the new edge has zero myosin on it according to observations of planar cell polarity in the tissue. In the current model, we have chosen $l_{\text{min}} = 0.1\ \mu\text{m}$, about 2.8% of the undeformed edge length l_0.

In two dimensions, the execution of the transition is straightforward. Three dimensionality brings a potential geometric complication. As myosin-based contraction happens on the apical surface but not the basal one, the intercalation criterion above will only be met on the apical surface. Then neighbor exchange on the apical surface alone may disrupt the correspondence between apical and basal nodes and cause intersection of elements [32]. To prevent this, we enforce a basal intercalation whenever an apical one occurs, even though the basal edge does not meet the threshold l_{min}. This ensures that the basal topology matches the apical topology and maintains the integrity of connectivity of the lateral edges.

S9 Supplementary Movies

Captions to the movies referenced in the main paper and the SI:

Movie S1: Deformation of the eccentric placode with no adhesion to the surrounding tissue. The left panel shows a top-down view of the placode while the right panel a cross-sectional view on the symmetry plane that cuts through the center of the pit. The apicomedial myosin inside the pit and the myosin arc closest to it onset at $t = 0$. The three outer myosin arcs onset at $t = 375$ s, and the circumferential actomyosin cable starts at $t = 3500$ s. All parameters are at their baseline values of Table S1.

Movie S2: Deformation of the eccentric placode with nonuniform adhesion to the surrounding tissue. Stronger adhesion bonds (elastic constant $k_{ad} = 100\ \text{nN}\,\mu\text{m}^{-1}$) are used on the two near-side edges closest to the pit, while weaker ones ($k_{sd} = 10\ \text{nN}\,\mu\text{m}^{-1}$) are on the two side edges. See Fig. S1 for the geometric setup. All other parameters are the same as in Movie S1.

Movie S3: Deformation of the eccentric placode with nonuniform adhesion to the surrounding tissue, with the cell and spoke elasticity softened to 1/4 of the default value: $\mu = 0.25\ \text{nN}\,\mu\text{m}^{-1}$. All other parameters are the same as in Movie S2.

Movie S4: Invagination of the concentric *in silico* wild-type placode using the baseline parameters of Table S1. The left panel shows a top-down view of the apical surface of the placode. The right panel shows a cross-sectional view on the mid-plane. The apicomedial myosin inside the pit (made of the innermost 7 cells) onsets at $t = 0$, as does the inner myosin arc. The outer myosin arc onsets at $t = 375$ s, and the circumferential actomyosin cable starts at $t = 3500$ s.

Movie S5: Invagination of the concentric placode with 4 edges undergoing intercalation. See Fig. 7 of the main paper for the geometric setup. The myosin on these 4 edges onset at $t = 375$ s, and the intercalations occur quickly afterward, between 400 and 410 s. All other parameters are the same as in Movie S4.

Movie S6: Invagination of the concentric placode with the cell and spoke elasticity softened to 1/4 of the default value: $\mu = 0.25\ \text{nN}\,\mu\text{m}^{-1}$. Note the multiple intercalations happening spontaneously in the invaginated pit from $t = 5270$ to 5290 s. The final configuration features a narrower lumen. All other parameters are the same as in Movie S4.

References

[1] Y. E. Sanchez-Corrales, G. B. Blanchard, K. Röper, Radially patterned cell behaviours during tube budding from an epithelium, eLife 7 (2018) 1–36.

[2] R. Clément, B. Dehapiot, C. Collinet, T. Lecuit, P. F. Lenne, Viscoelastic dissipation stabilizes cell shape changes during tissue morphogenesis, Curr. Biol. 27 (2017) 3132–3142.e4.

[3] K. V. Iyer, R. Piscitello-Gómez, J. Paijmans, F. Jülicher, S. Eaton, Epithelial viscoelasticity is regulated by mechanosensitive E-cadherin turnover, Curr. Biol. 29 (2019) 578–591.e5.

[4] R. J. Tetley, G. B. Blanchard, A. G. Fletcher, R. J. Adams, B. Sanson, Unipolar distributions of junctional Myosin II identify cell stripe boundaries that drive cell intercalation throughout *Drosophila* axis extension, eLife 5 (2016) e12094.

[5] R. Magno, V. A. Grieneisen, A. F. Marée, The biophysical nature of cells: Potential cell behaviours revealed by analytical and computational studies of cell surface mechanics, BMC Biophys. 8 (1) (2015) 8.

[6] Q. Wang, J. J. Feng, L. M. Pismen, A cell-level biomechanical model of *Drosophila* dorsal closure, Biophys. J. 103 (11) (2012) 2265–2274.

[7] C. Durney, T. Harris, J. Feng, Dynamics of PAR proteins explain the oscillation and ratcheting mechanisms in dorsal closure, Biophys. J. 115 (11) (2018) 2230–2241.

[8] X. Du, M. Osterfield, S. Y. Shvartsman, Computational analysis of three-dimensional epithelial morphogenesis using vertex models, Phys. Biol. 12 (1) (2015) 019501.

[9] N. Murisic, V. Hakim, I. G. Kevrekidis, S. Y. Shvartsman, B. Audoly, From discrete to continuum models of three-dimensional deformations in epithelial sheets, Biophys. J. 109 (1) (2015) 154–163.

[10] G. C. Girdler, K. Röper, Controlling cell shape changes during salivary gland tube formation in *Drosophila*, Semin. Cell Dev. Biol. 31 (2014) 74–81.

[11] S. Chung, C. D. Hanlon, D. J. Andrew, Building and specializing epithelial tubular organs: The *Drosophila* salivary gland as a model system for revealing how epithelial organs are specified, form and specialize, Dev. Biol. 3 (4) (2014) 281–300.

[12] J. Solon, A. Kaya-Çopur, J. Colombelli, D. Brunner, Pulsed forces timed by a ratchet-like mechanism drive directed tissue movement during dorsal closure, Cell 137 (7) (2009) 1331–1342.

[13] L. A. Davidson, G. F. Oster, R. E. Keller, M. A. Koehl, Measurements of mechanical properties of the blastula wall reveal which hypothesized mechanisms of primary invagination are physically plausible in the sea urchin *Strongylocentrotus purpuratus*, Dev. Biol. 209 (2) (1999) 221–238.

[14] E. Roan, K. R. Wilhelm, C. M. Waters, Kymographic imaging of the elastic modulus of epithelial cells during the onset of migration, Biophys. J. 109 (10) (2015) 2051–2057.

[15] E. Hannezo, J. Prost, J.-F. Joanny, Theory of epithelial sheet morphology in three dimensions, PNAS 111 (1) (2014) 27–32.

[16] R. Phillips, J. Kondev, J. Theriot, H. Garcia, Physical Biology of the Cell, Garland Science, 2012.

[17] G. Forgacs, R. A. Foty, Y. Shafrir, M. S. Steinberg, Viscoelastic properties of living embryonic tissues: A quantitative study, Biophys. J. 74 (5) (1998) 2227–2234.

[18] A. Besser, U. S. Schwarz, Coupling biochemistry and mechanics in cell adhesion: A model for inhomogeneous stress fiber contraction, New J. Phys. 9 (2007) 1367–2630.

[19] S. Chung, S. Kim, D. J. Andrew, Uncoupling apical constriction from tissue invagination, eLife 6 (2017) 1–25.

[20] T. Q. Uyeda, S. J. Kron, J. A. Spudich, Myosin step size: Estimation from slow sliding movement of actin over low densities of heavy meromyosin, J. Mol. Biol. 214 (3) (1990) 699 – 710.

[21] M. Vinzenz, M. Nemethova, F. Schur, J. Mueller, A. Narita, E. Urban, C. Winkler, C. Schmeiser, S. A. Koestler, K. Rottner, G. P. Resch, Y. Maeda, J. V. Small, Actin branching in the initiation and maintenance of lamellipodia, J. Cell Sci. 125 (11) (2012) 2775–2785.

[22] K. Röper, Anisotropy of Crumbs and aPKC drives myosin cable assembly during tube formation, Dev. Cell 23 (5) (2012) 939–953.

[23] T. Brody, The interactive fly: gene networks, development and the internet, Trends Genet. 15 (8) (1990) 333–334.

[24] N. Guz, M. Dokukin, V. Kalaparthi, I. Sokolov, If cell mechanics can be described by elastic modulus: study of different models and probes used in indentation experiments, Biophys. J. 107 (3) (2014) 564–575.

[25] R. T. Adkins, Information Sources in Polymers and Plastics, Bowker-Saur, 1989.

[26] S. Kalpakjian, S. Schmid, Manufacturing Processes for Engineering Materials, Pearson, 2016.

[27] L. He, X. Wang, H. L. Tang, D. J. Montell, Tissue elongation requires oscillating contractions of a basal actomyosin network, Nat. Cell Biol. 12 (12) (2010) 1133–1142.

[28] K. E. Kasza, J. A. Zallen, Dynamics and regulation of contractile actin–myosin networks in morphogenesis, Curr. Opin. Cell Biol. 23 (1) (2011) 30–38.

[29] T. Luo, K. Mohan, V. Srivastava, Y. Ren, P. A. Iglesias, D. N. Robinson, Understanding the cooperative interaction between myosin ii and actin cross-linkers mediated by actin filaments during mechanosensation, Biophys. J. 102 (2) (2012) 238–247.

[30] S. Alt, P. Ganguly, G. Salbreux, Vertex models: From cell mechanics to tissue morphogenesis, Phil. Trans. R. Soc. B 372 (1720) (2017) 20150520.

[31] L. C. Siang, R. Fernandez-Gonzalez, J. J. Feng, Modeling cell intercalation during *Drosophila* germband extension, Phys. Biol. 15 (6) (2018) 066008.

[32] A. G. Fletcher, J. M. Osborne, P. K. Maini, D. J. Gavaghan, Implementing vertex dynamics models of cell populations in biology within a consistent computational framework, Prog. Biophys. Mol. Biol. 113 (2) (2013) 299–326.

[33] H. Lan, Q. Wang, R. Fernandez-Gonzalez, J. J. Feng, A biomechanical model for cell polarization and intercalation during *Drosophila* germband extension, Phys. Biol. 12 (5) (2015) 056011.